University of Thessaly
School of Engineering
Department of Mechanical Engineering

Diploma Thesis

Finite Element Analysis of the Automotive Crash Box Impact Test

by

ATHANASIOS GIOTAS

Submitted in Partial Fulfilment of the
Requirements for Diploma in Mechanical Engineering
2021

Approved by the Three Members of the Advisory Committee:

First Member (Supervisor)

Professor Nikolaos Aravas
Department of Mechanical Engineering, University of Thessaly

Second Member

Professor Grigorios Haidemenopoulos
Department of Mechanical Engineering, University of Thessaly

Third Member

Dr. Ioanna Papadioti
Department of Mechanical Engineering, University of Thessaly

Abstract

Finite Element Analysis of the Automotive Crash Box Impact Test

Athanasios Giotas

Supervisor: Professor N. Aravas

This work is concerned with the examination of the effect of non-local theories in the numerical simulation of the crash box impact test. The effect of interactions from areas distant from the material point we examine can be included through the introduction of the non-local equivalent plastic strain e^p and the solution of the respective boundary value problem, which includes a "material length" ℓ added to the constitutive equations. The fundamentals of damage modeling, the local and non-local theories, as well as the numerical integration of the constitutive model and the treatment of non-local dynamic problems in a computational environment are covered. The non-local effects are explored in the application of the crash box and the results of the simulation are cited. The analysis of the model was carried out with the use of a VUMAT user subroutine and the ABAQUS/Explicit solver, provided by the general purpose finite element program ABAQUS.

Keywords: Gradient Plasticity; Finite Element Method; Crash box;

Acknowledgements

I would deeply like to thank my supervisor, Professor Nikolaos Aravas, whose great knowledge and expertise in the subjects of Mechanics of Materials and Computational Mechanics inspired me greatly to follow this particular field.

I also wish to thank Dr. Ioanna Papadioti for providing the theoretical basis and relevant algorithms for the numerical simulation of the model examined in this thesis.

Finally, I am extremely grateful to PhD student in the Department of Mechanical Engineering, Socrates Xenos, for his valuable help and guidance throughout this project.

Contents

List of Figures

Introduction

Classical continuum models can be considered *local*, in the sense that they do not take into consideration interactions from long-distance material points and accept force interactions only in the form of body forces at a finite distance. As long as no discontinuities are present and the strain distribution is smooth, the consideration mentioned above poses no problems. However, in the case of highly non-linear (inelastic) material behavior (i.e., strain localization due to severe plastic deformation), classical continuum models that do not include a characteristic length are insufficient and therefore fail to produce meaningful results. This makes it very important to develop and use enhanced models, where the long-distance interactions are dictated by the characteristic length ℓ of the material.

A basic development of damage modelling was introduced by Bai and Wierzbicki [3], [5], [6], whose works are a very useful guide for the damage model used throughout this thesis. The studies of Lian *et al.*(2012) [11] and Wu *et al.*(2017) [18] described a modified version of the Bai-Wierzbicki damage model, which, along with the definition of the boundary value problem for the non-local equivalent plastic strain e^p used in Peerlings *et al.*(2001) [15] and Engelen *et al.*(2003) [8] and some alterations made by Papadioti *et al.*(2019) [14] provide the tools needed to solve the problems mentioned above.

In the context of this thesis, the modified BW (MBW) model mentioned previously will be used for the numerical simulation of the well-known automotive crash box impact test. For the constitutive modeling of the underlying material microstructure, both the local and non-local versions of the model as presented in Papadioti *et al.*(2019) [14] will be used. The efficacy of the corresponding non-local model on the alleviation of the computational issues that appear in FE analyses of softening and damage is thoroughly examined.

In Chapter 1, fundamental elements of continuum mechanics that are used in the subsequent constitutive modeling are briefly described.

In Chapter 2, the local and non-local theories are presented, along with some classic versions of the damage model that is used for this thesis, and the numerical solution process that is followed in order to obtain the desired results. A description of the Crash Box Impact Test, together with the results of the numerical analysis, as well as a discussion on them are the main contents of Chapter 3. Finally, Chapter 4 makes a brief summary of the topics of this thesis and draws some basic conclusions.

Standard notation is used throughout this work. Boldface symbols denote tensors the orders of which are indicated by the context. All tensor components are written with respect to a fixed Cartesian coordinate system with base vectors $\mathbf{e}_i$ $(i = 1, 2, 3)$, and the summation convention is used for repeated Latin indices, unless otherwise indicated. The prefice det indicates the determinant, a superscript T the transpose, a superposed dot the material time derivative, and the superscripts *sym* and *skew*, enclosed in parentheses, the symmetric and anti-symmetric parts of a second order tensor. Let $\mathbf{a}$, $\mathbf{b}$ be vectors, $\mathbf{A}$, $\mathbf{B}$ second-order tensors, and $\boldsymbol{\mathcal{C}}$, $\boldsymbol{\mathcal{D}}$ two fourth-order tensors; the following products are used in the text: $(\mathbf{a}\,\mathbf{b})_{ij} = a_i\, b_j$, $\mathbf{A} : \mathbf{B} = A_{ij}\, B_{ij}$, $(\mathbf{A}\cdot\mathbf{B})_{ij} = A_{ik}\, B_{kj}$, $(\mathbf{A}\,\mathbf{B})_{ijkl} = A_{ij}\, B_{kl}$, $(\boldsymbol{\mathcal{C}} : \mathbf{A})_{ij} = \mathcal{C}_{ijkl}\, A_{kl}$, and $(\boldsymbol{\mathcal{C}} : \boldsymbol{\mathcal{D}})_{ijkl} = \mathcal{C}_{ijpq}\, \mathcal{D}_{pqkl}$. The inverse $\boldsymbol{\mathcal{C}}^{-1}$ of a fourth-order tensor $\boldsymbol{\mathcal{C}}$ that has the "minor" symmetries $\mathcal{C}_{ijkl} = \mathcal{C}_{jikl} = \mathcal{C}_{ijlk}$ is defined so that $\boldsymbol{\mathcal{C}} : \boldsymbol{\mathcal{C}}^{-1} = \boldsymbol{\mathcal{C}}^{-1} : \boldsymbol{\mathcal{C}} = \boldsymbol{\mathcal{I}}$, where $\boldsymbol{\mathcal{I}}$ is the symmetric fourth-order identity tensor with Cartesian components $\mathcal{I}_{ijkl} = (\delta_{ik}\,\delta_{jl} + \delta_{il}\,\delta_{jk})/2$, δ_{ij} being the Kronecker delta.

Chapter 1

Basic Theory of Continuum Mechanics

1.1 The Polar Decomposition Theorem

If $\mathbf{A}$ is invertible second order tensor, it can be shown that $\mathbf{A}$ can be uniquely right or left multiplicatively decomposed into two tensors:

$$\mathbf{A} = \mathbf{Q} \cdot \mathbf{U} = \mathbf{V} \cdot \mathbf{Q} \tag{1.1}$$

with $\mathbf{Q}$ being an orthogonal second order tensor, and $\mathbf{U}, \mathbf{V}$ being second order symmetric and positive definite tensors. Equation (1.1) is known as the *polar decomposition theorem*. As symmetric and positive definite tensores, $\mathbf{U}$ and $\mathbf{V}$ have real and positive eigenvalues which means that $\det \mathbf{U}, \det \mathbf{U}^{-1} > 0$ and $\det \mathbf{V}, \det \mathbf{V}^{-1} > 0$.
Using the polar decomposition theorem, the deformation gradient $\mathbf{F}$ can be multiplicatively decomposed and be written as:

$$\mathbf{F} = \mathbf{Q} \cdot \mathbf{U} = \mathbf{V} \cdot \mathbf{Q} \tag{1.2}$$

Solving for $\mathbf{Q}$ in (1.2) and calculating its determinant:

$$\det \mathbf{Q} = \det \mathbf{F} \det \mathbf{U}^{-1}, \tag{1.3}$$

and since $\det \mathbf{F} = J > 0$, then $\det \mathbf{Q} > 0$. This means that $\mathbf{Q}$ is a proper orthogonal tensor, i.e. $\mathbf{Q}$ is a rotation tensor which will from here on be denoted as $\mathbf{R}$. Thus, equation (1.3) can be written as:

$$\mathbf{F} = \mathbf{R} \cdot \mathbf{U} = \mathbf{V} \cdot \mathbf{R} \tag{1.4}$$

where tensors $\mathbf{U}$ and $\mathbf{V}$ are defined as:

$$\mathbf{U} = \sqrt{\mathbf{C}} \quad \text{and} \quad \mathbf{V} = \sqrt{\mathbf{B}}, \tag{1.5}$$

with $\mathbf{C}$ and $\mathbf{B}$ being symmetric and positive definite second order tensors known as *right*

and *left Cauchy-Green* tensors respectively, as:

$$\mathbf{C} = \mathbf{F}^T \cdot \mathbf{F} \quad \text{and} \quad \mathbf{B} = \mathbf{F} \cdot \mathbf{F}^T. \tag{1.6}$$

1.2 Generalized Strain Measures

Based on the classical theory of small strains, the (nominal) deformation of a material fiber with a reference length ds_0 that is stretched to a length ds is:

$$\varepsilon = \frac{ds - ds_0}{ds_0} = \frac{ds}{ds_0} - 1 = \lambda - 1 \tag{1.7}$$

where λ is the stretch ratio defined as $\lambda = \frac{ds}{ds_0} = \sqrt{\mathbf{N} \cdot \mathbf{C} \cdot \mathbf{N}}$, where $\mathbf{C}$ is the aforementioned left Cauchy-Green tensor and $\mathbf{N}$ is the direction of the material fiber in the undeformed state. Equation (1.7) is viable for small strain, one-dimensional deformations, however, in the case of generalized finite three-dimensional geometrical variations, a more general description of deformation is needed. Thus, general families of strain tensors either with respect to the reference or current configuration, known as Langragian and Eulerian strain tensors respectively can be defined:

$$\mathbf{E}^{(m)}(\lambda_i) = \sum_{i=1}^{3} f^{(m)}(\lambda_i) \mathbf{N}_i \mathbf{N}_i \tag{1.8}$$

$$\mathbf{e}^{(m)}(\lambda_i) = \sum_{i=1}^{3} f^{(m)}(\lambda_i) \mathbf{n}_i \mathbf{n}_i \tag{1.9}$$

where:

$$f^{(m)}(\lambda) = \begin{cases} \frac{1}{m}(\lambda^m - 1) & , \quad m \neq 0 \\ \ln(\lambda) & , \quad m = 0 \end{cases} \qquad m \in \mathbb{Z}$$

It can be shown that $\mathbf{E}^{(m)}(\lambda)$ can be written as:

$$\mathbf{E}^{(m)} = \begin{cases} \frac{1}{m}[(\mathbf{F}^T \cdot \mathbf{F})^n - \boldsymbol{\delta}] & , \qquad m = 2n \\ \frac{1}{m}[(\mathbf{F}^T \cdot \mathbf{F})^n \sqrt{\mathbf{F}^T \cdot \mathbf{F}} - \boldsymbol{\delta}] & , \qquad m = 2n + 1 \end{cases} \tag{1.10}$$

where $n \in \mathbb{Z}$.
In the case of $m = 0$, the resulting tensor (and one of the most common ones) is known as the *Hencky* or *logarithmic* strain tensor:

$$\mathbf{E}^{(\ln)} = \mathbf{E}^{(0)} = \ln \mathbf{U}, \quad \text{and} \tag{1.11}$$

$$\mathbf{e}^{(ln)} = \mathbf{e}^{(0)} = \ln \mathbf{V} \tag{1.12}$$

1.3 Rate of Deformation

As far as the deformation of a continuum body is concerned, apart from determining its deformation in a specific moment in time, the evolution of its deformation in time is very important as well. This is of utmost importance in cases of non-linear material behavior (i.e., plasticity), where the response of the material is affected by the deformation history.

The velocity of a continuum body can be expressed as:

$$\boldsymbol{v} = \frac{\partial \boldsymbol{x}(\boldsymbol{X}, t)}{\partial t} = \hat{\boldsymbol{v}}(\boldsymbol{X}, t) = \bar{\boldsymbol{v}}(\boldsymbol{x}, t) \tag{1.13}$$

where $\boldsymbol{X}$ is the position vector of a point in the body at the reference state, and $\boldsymbol{x}$ is the position vector of the same point in the current state.

Then, a spatial variation of the velocity, called *velocity gradient* tensor $\mathbf{L}$ can be defined as:

$$\mathbf{L} = \frac{\partial \boldsymbol{v}(\boldsymbol{x}, t)}{\partial \boldsymbol{x}} = \boldsymbol{v} \nabla_{\boldsymbol{x}} \tag{1.14}$$

In addition, the symmetric and anti-symmetric parts of tensor $\mathbf{L}$, called *deformation rate* ($\mathbf{D}$) and *spin* ($\mathbf{W}$) tensors respectively are defined as:

$$\mathbf{D} = \mathbf{L}^{(s)} = \frac{1}{2}(\mathbf{L} + \mathbf{L}^T) \text{ or } D_{ij} = \frac{1}{2}\left(\frac{\partial v_i}{\partial x_j} + \frac{\partial v_j}{\partial x_i}\right) \tag{1.15}$$

$$\mathbf{W} = \mathbf{L}^{(a)} = \frac{1}{2}(\mathbf{L} - \mathbf{L}^T) \text{ or } W_{ij} = \frac{1}{2}\left(\frac{\partial v_i}{\partial x_j} - \frac{\partial v_j}{\partial x_i}\right) \tag{1.16}$$

so that

$$\mathbf{L} = \mathbf{D} + \mathbf{W} \tag{1.17}$$

where s and a in equation (1.16) denote the symmetric and anti-symmetric part respectively.

Chapter 2

Fundamentals of Local and Non-Local Theories

An Eulerian formulation is used in the present thesis; both the kinematic and the constitutive equations are written in the current deformed state of the body. The elastic and plastic material response are treated separately and are later combined to obtain the total elastoplastic response. The deformation-rate tensor D at every point of the continuum is written as:

$$\mathbf{D} = \mathbf{D}^e + \mathbf{D}^p, \tag{2.1}$$

where $\mathbf{D}^e$ and $\mathbf{D}^p$ are the elastic and plastic parts respectively.

2.1 Elasticity

The elastic part of the deformation-rate tensor is assumed to be of isotropic linear hypoelastic form. This means that:

$$\mathbf{D}^e = \boldsymbol{\mathcal{M}}^e : \overset{\triangledown}{\boldsymbol{\sigma}} \qquad \text{or} \qquad \overset{\triangledown}{\boldsymbol{\sigma}} = \boldsymbol{\mathcal{L}}^e : \mathbf{D}^e \tag{2.2}$$

where $\overset{\triangledown}{\boldsymbol{\sigma}}$ is the Jaumann or co-rotational rate of the stress tensor,

$$\boldsymbol{\mathcal{M}}^e = \frac{1}{2G}\boldsymbol{\mathcal{K}} + \frac{1}{3\kappa}\boldsymbol{\mathcal{J}}, \quad \boldsymbol{\mathcal{L}}^e = (\boldsymbol{\mathcal{M}}^e)^{-1} = 2G\boldsymbol{\mathcal{K}} + 3\kappa\boldsymbol{\mathcal{J}}, \quad \boldsymbol{\mathcal{J}} = \frac{1}{3}\boldsymbol{\delta}\boldsymbol{\delta}, \quad \boldsymbol{\mathcal{K}} = \boldsymbol{\mathcal{I}} - \boldsymbol{\mathcal{J}}, \tag{2.3}$$

(G,κ) are the elastic shear and bulk moduli respectively, $\boldsymbol{\delta}$ and $\boldsymbol{\mathcal{I}}$ the the second- and fourth-order identity tensors with Cartesian components δ_{ij} (the Kronecker delta) and $\mathcal{I}_{ijkl} = \frac{1}{2}(\delta_{ik}\delta_{jl} + \delta_{il}\delta_{jk})$.

2.2 Plasticity

The yield function is isotropic and the corresponding yield criterion is given as:

$$\Phi(p, \sigma_e, \theta, \bar{e}^p, D) = 0, \tag{2.4}$$

where $\boldsymbol{\sigma}$ is the true (Cauchy) stress tensor, p = $\frac{1}{3}\sigma_{kk}$ the hydro-static stress, $\boldsymbol{s} = \boldsymbol{\sigma} - p\boldsymbol{\delta}$ the stress deviator, $\sigma_e = \sqrt{\frac{3}{2}\boldsymbol{\sigma} : \boldsymbol{\sigma}}$ the von Mises equivalent stress, $J_3 = \frac{1}{3}\ \mathrm{tr}(\boldsymbol{\sigma}^3)$=det$\boldsymbol{\sigma}$, θ the "Lode angle" defined by

$$3\theta = \arcsin\left(\frac{-27}{2}\frac{J_3}{\sigma_e^3}\right), \qquad -\frac{\pi}{2} \leq 3\theta \leq \frac{\pi}{2} \tag{2.5}$$

D is a "damage parameter" that takes values between 0 and 1, and $\bar{\varepsilon}^p$ the von Mises equivalent plastic strain, the rate of which is defined as

$$\dot{\bar{\varepsilon}}^p = \sqrt{\frac{2}{3}\mathbf{D}^p : \mathbf{D}^p}. \tag{2.6}$$

For the Lode angle, the values $\theta = 0$, $\theta = \frac{\pi}{6}$ and $\theta = -\frac{\pi}{6}$ correspond to pure shear, uniaxial compression and uniaxial tension respectively. Two more parameters, the "normalized Lode angle" $\bar{\theta}$ and the stress triaxiality η are defined as well:

$$\eta = \frac{p}{\sigma_e}, \qquad \bar{\theta} = -\frac{\theta}{\pi/6} \tag{2.7}$$

with the values of $\bar{\theta}$ being $\bar{\theta} = 0$ in pure shear, $\bar{\theta} = 1$ in uniaxial tension and $\bar{\theta} = -1$ in uniaxial compression.

The normality rule defines the plastic part of the deformation rate tensor $\mathbf{D}^p$:

$$\mathbf{D}^p = \dot{\lambda}\mathbf{P}, \qquad \mathbf{P} = \frac{\partial \Phi}{\partial \sigma}, \tag{2.8}$$

where $\dot{\lambda}$ is a non-negative plastic flow parameter. Thus,

$$\dot{\bar{\varepsilon}}^p = \dot{\lambda}\bar{P}, \qquad \bar{P} = \sqrt{\frac{2}{3}\mathbf{P} : \mathbf{P}} \tag{2.9}$$

and the normal $\mathbf{P}$ to the smooth yield surface can be written as:

$$\mathbf{P} = \frac{\partial \Phi}{\partial \sigma} = \frac{\partial \Phi}{\partial p}\frac{\partial p}{\partial \boldsymbol{\sigma}} + \frac{\partial \Phi}{\partial \sigma_e}\frac{\partial \sigma_e}{\partial \boldsymbol{\sigma}} + \frac{\partial \Phi}{\partial \theta}\frac{\partial \theta}{\partial \boldsymbol{\sigma}} = \frac{1}{3}\frac{\partial \Phi}{\partial p}\boldsymbol{\delta} + \frac{\partial \Phi}{\partial \sigma_e}\mathbf{N} + \frac{1}{\sigma_e}\frac{\partial \Phi}{\partial \theta}\mathbf{M}, \tag{2.10}$$

where

$$\mathbf{N} = \frac{\partial \sigma_e}{\partial \sigma} = \frac{3}{2\sigma_e}\boldsymbol{\sigma}, \qquad \mathbf{M} = \sigma_e \frac{\partial \theta}{\partial \sigma} = \frac{1}{\cos 3\theta}(\boldsymbol{\delta} - \sin 3\theta \mathbf{N} - 2\mathbf{N}^2) \tag{2.11}$$

Remarks

1. The principal directions of $\boldsymbol{\sigma}, \boldsymbol{s}, \mathbf{N}, \mathbf{M}, \mathbf{P}$ and $\mathbf{D}^p$ are coincidental (and are called coaxial), as shown by the equations (2.8), (2.10) and (2.11)

2. The dimensionless "direction tensors" $\boldsymbol{\delta}, \mathbf{N}$ and $\mathbf{M}$, which are orthogonal and have constant magnitude are used to define the normal $\mathbf{P}$ to the yield surface in (2.10). For the "direction tensors":

$$\boldsymbol{\delta} : \boldsymbol{\delta} = 3, \qquad \mathbf{N} : \mathbf{N} = \mathbf{M} : \mathbf{M} = \frac{3}{2}, \qquad \mathbf{N} : \boldsymbol{\delta} = \mathbf{M} : \boldsymbol{\delta} = \mathbf{N} : \mathbf{M} = 0 \tag{2.12}$$

   and $\mathbf{N}$ and $\mathbf{M}$ are deviatoric ($N_{kk} = M_{kk} = 0$).
   In the space of principal stresses $(\sigma_1, \sigma_2, \sigma_3)$ in Figure 2.1, tensors $(\boldsymbol{\delta}, \mathbf{N}, \mathbf{M})$ are shown as vectors $(\boldsymbol{\delta}^v, \mathbf{N}^v, \mathbf{M}^v)$. The equation $\sigma_1 + \sigma_2 + \sigma_3 = 0$ on the $(\sigma_1, \sigma_2, \sigma_3)$ space is used to define the deviatoric Π- plane. $\boldsymbol{\delta}^v$ is the vector normal to the Π- plane, whereas $\mathbf{N}^v$ and $\mathbf{M}^v$ lie on the plane and are perpendicular to each other.

3. Special treatment is needed in the definition of $\mathbf{M}$ in equation (2.11b) when $\theta \to \pm\frac{\pi}{6}$, since in that case $\cos 3\theta \to 0$. This specific case is analysed in Papadioti *et al.*(2019) [14] (Section 2.2.1), where it is shown that on smooth yield surfaces, $\mathbf{M}$ approaches unique finite values as $\theta \to \pm\frac{\pi}{6}$.

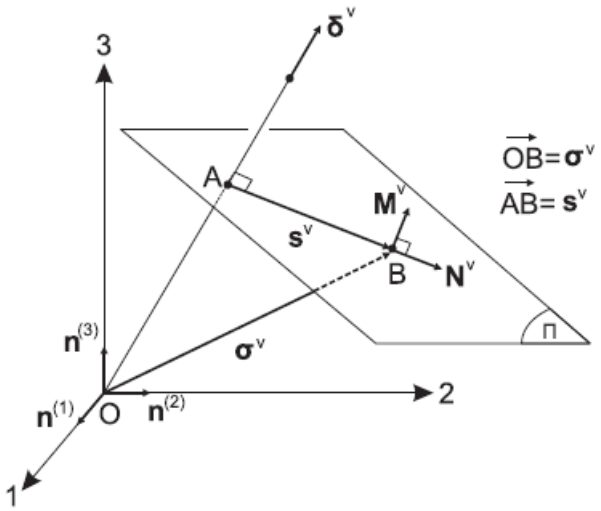

Figure 2.1: Schematic representation of $\boldsymbol{\sigma}^v, \boldsymbol{\sigma}^v, \boldsymbol{\delta}^v, \mathbf{N}^v$ and $\mathbf{M}^v$ in the principal coordinate system for $\sigma_1 \geq \sigma_2 \geq \sigma_3$. When $\sigma_1 \leq \sigma_2 \leq \sigma_3$, $\mathbf{M}^v$ has the opposite direction of that shown.

2.3 Damage modeling

2.3.1 Bai and Wierzbicki (BW) damage model

In their paper, Bai and Wierzbicki [3] discuss various commonly used failure criteria for metals. These criteria suggest that fracture occurs at a point in a body when:

$$\int_0^{\bar{\varepsilon}^p} \frac{d\bar{\varepsilon}^p}{f(\eta,\theta)} \tag{2.13}$$

reaches a critical value at that point where $f(\eta,\theta)$ is a dimensionless strain-dependent weighting function. They suggest to normalize $f(\eta,\theta)$ in order for this critical value to be equal to unity (BW model). Thus we can write:

$$D(\bar{\varepsilon}^p_f) = 1, \quad \text{with} \quad D(\bar{\varepsilon}^p) = \int_0^{\bar{\varepsilon}^p} \frac{d\bar{\varepsilon}^p}{f(\eta,\theta)}\,, \tag{2.14}$$

where $\bar{\varepsilon}^p$ is the value of $\bar{\varepsilon}^p_f$ when the fracture occurs. D can be thought of as a "damage indicator".

2.3.2 The Modified Bai and Wierzbicki (MBW) damage model

In a physical sense, damage initiation at a material point is identified with the creation of a micro-defect (e.g., a microcrack) at that point. When the material deforms plastically, i.e., when $\bar{\varepsilon}^p$ is non zero, damage starts accumulating. Based on experimental data, Lian *et al.*[11] and Wu *et al.*[18] suggested that damage does not initiate at $\bar{\varepsilon}^p = 0$ and instead they define the "damage initiation indicator" I:

$$I = \int_0^{\bar{\varepsilon}^p} \frac{d\bar{\varepsilon}^p}{\bar{\varepsilon}^p_i(\eta_{av},\bar{\theta}_{av})}\,, \quad \eta_{av} = \frac{1}{\bar{\varepsilon}^p}\int_0^{\bar{\varepsilon}^p} \eta\, d\bar{\varepsilon}^p, \quad \bar{\theta}_{av} = \frac{1}{\bar{\varepsilon}^p}\int_0^{\bar{\varepsilon}^p} \bar{\theta}_{av}\, d\bar{\varepsilon}^p, \tag{2.15}$$

where $\bar{\theta}$ is the normalized Lode angle defined in (2.7),

$$\bar{\varepsilon}^p_i = (c_1 e^{-c_2\eta_{av}} - c_3 e^{-c_4\eta_{av}})\bar{\theta}^2_{av} + c_3 e^{-c_4\eta_{av}},$$

and (c_1, c_2, c_3, c_4) are dimensionless positive material constants.
When $I = 1$, damage is assumed to initiate and if parameters (η,θ) are constant in a loading program (proportional loading), then damage initiation occurs when $\bar{\varepsilon}^p = \bar{\varepsilon}^p_i(\eta,\theta)$.
In the case of general, non-proportional loading, we let σ_{yi} denote the value of the material flow stress σ_y when $I = 1$ (damage initiation). Once $I = 1$, the damage parameter D starts

evolving according to the following relation:

$$\dot{D} = \begin{cases} \frac{\sigma_{yi}}{G_f}\dot{\bar{\varepsilon}}^p & if \quad I = 1 \quad and \quad \eta > \eta_{cr} \\ 0 \quad \text{otherwise} \end{cases} \tag{2.16}$$

where G_f is a material parameter with dimensions of energy per unit volume, η_{cr} is a critical value of stress triaxiality below which local material failure never occurs ($\eta_{cr} \simeq -\frac{1}{3}$, Bai and Wierzbicki (2005) [4]), and

$$D_{cr}(\eta_{av}, \bar{\theta}_{av}) = \min[(c_5 e^{-c_6\eta_{av}} - c_7 e^{-c_8\eta_{av}})\bar{\theta}_{av}^2 + c_7 e^{-c_8\eta_{av}}, D_{max}], \tag{2.17}$$

(c_5, c_6, c_7, c_8) are dimensionless positive material constants, and D_{max} an upper limit to the "damage parameter" D to make sure that D_{cr} is always $\leqslant 1$ ($D_{max} \lesssim 1$).
Wu *et al.*(2017) [18] introduce the "failure indicator" I_f, for which:

$$\dot{I}_f = \frac{\dot{D}}{D_{cr}(\eta_{av}, \theta_{av})}. \tag{2.18}$$

Local material failure occurs when $I_f = 1$.

2.4 Non-local formulation

As discussed in the introduction, a characteristic problem in damage mechanics models is the fact that, when the material enters the softening region, before its failure, the results that finite element analyses produce may be unreliable, due to the dependency on the mesh size. In order to solve this problem, various theories have been developed, a popular one being the "non-local", or "strain-gradient" theory. In this theory, a "non local equivalent plastic strain" e^p is introduced and a "strain gradient" version of the MBW model is developed.

2.4.1 Non-local equivalent plastic strain gradient formulation

According to Peerlings *et al.*(2001) [15], and Engelen *et al.*(2003) [8], the "non local" equivalent plastic strain field $e^p(\mathbf{x})$ in terms of the "local" equivalent plastic strain field is defined when solving the following boundary value problem (BVP):

$$e^p - \ell^2\nabla^2 e^p = \bar{\varepsilon}^p \qquad in \quad \Omega \tag{2.19}$$

$$\frac{\partial e^p}{\partial n} \equiv \mathbf{n}\cdot\nabla e^p = 0 \qquad on \quad \partial\Omega, \tag{2.20}$$

where ℓ is a material parameter with dimensions of length, Ω is the domain occupied by the elastoplastic body in its deformed state, $\partial\Omega$ is the body's boundary and $\mathbf{n}$ the unit outward normal vector to $\partial\Omega$. The boundary condition (2.20) guarantees that the "total values" of

e^p and $\bar{\varepsilon}^p$ in Ω are coincidental.

By solving the above BVP, the non-local equivalent plastic strain e^p is determined in the ***entire problem domain*** Ω and not just inside the plastic zone, according to Peerlings *et al.*(2001) [15]; Engelen *et al.*(2003) [8]. Based on their work, and some slightly different but important interpretation by Papadioti *et al.*(2019) [14], we end up with the following equation:

$$\bar{\varepsilon}^p_{av}(\mathbf{x}) - \ell^2\nabla^2\bar{\varepsilon}^p_{av}(\mathbf{x}) = \bar{\varepsilon}^p(\mathbf{x}) + O(\ell^4\nabla^4\bar{\varepsilon}^p), \tag{2.21}$$

where $\bar{\varepsilon}^p_{av}$ is the average value of the local equivalent plastic strain $\bar{\varepsilon}^p$ over a material sphere V of radius R centered at $\mathbf{x}$, and $\ell = \frac{R}{\sqrt{10}}$.

Comparison of (2.21) with (2.19) draws the conclusion that the non-local equivalent plastic strain $e^p(\mathbf{x})$ in (2.19) can be identified with the average value $\bar{\varepsilon}^p_{av}(\mathbf{x})$ of the local equivalent plastic strain $\bar{\varepsilon}^p$ over a *circle* of radius $R = \sqrt{10}\ell = 3.16\ell$, centered at $\mathbf{x}$, to within terms $O(\ell^4\nabla^4\bar{\varepsilon}^p)$.

Following a similar approach, it can be shown that in two dimensional problems, the non-local equivalent plastic strain $e^p(\mathbf{x})$ can be identified with the average value $\bar{\varepsilon}^p_{av}$ of the local equivalent plastic strain $\bar{\varepsilon}^p$ over a circle of radius $R = 2\sqrt{2}\ell = 2.83\ell$ centered at $\mathbf{x}$, to within terms $O(\ell^4\nabla^4\bar{\varepsilon}^p)$.

2.4.2 The non-local version of MBW

In this work, a non-local version of the MBW damage model is used, in which the local equivalent plastic strain $\bar{\varepsilon}^p$ is replaced by the non-local equivalent plastic strain $\bar{e}^p$ in all expressions of 2.3.2. Thus, the value of damage D at a material point is not determined by the value of the local equivalent plastic strain $\bar{e}^p$ at that point. Instead, D is calculated at a certain material point by using the average value of the non-local equivalent plastic strain $\bar{\varepsilon}^p$ over a material sphere of radius of about 3ℓ, centered at that point. In particular:

$$\dot{I} = \frac{\dot{\hat{e}}^p}{\bar{\varepsilon}^p_i(\eta_{av}, \bar{\theta}_{av})}, \quad \eta_{av} = \frac{1}{\hat{e}^p}\int_0^{\hat{e}^p}\eta d\hat{e}^p\,, \quad \bar{\theta}_{av} = \frac{1}{\hat{e}^p}\int_0^{\hat{e}^p}\theta d\hat{e}^p \tag{2.22}$$

$$\dot{D} = \alpha\frac{\sigma_{yi}}{G_f}\dot{\hat{e}}^p, \quad \alpha = \begin{cases} 1 & \text{if} \quad I = 1 \quad \text{and} \quad \eta > \eta_{cr} \\ 0 & \text{otherwise} \end{cases} \tag{2.23}$$

$$\dot{I}_f = \frac{\dot{D}}{D_{cr}(\eta_{av}, \theta_{av})}, \tag{2.24}$$

where $\bar{\varepsilon}^p_i(\eta_{av}, \bar{\theta}_{av})$ is defined by

$$\bar{\varepsilon}^p_i = (c_1 e^{-c_2\eta_{av}} - c_3 e^{-c_4\eta_{av}})\bar{\theta}^2_{av} + c_3 e^{-c_4\eta_{av}}, \tag{2.25}$$

and $D_{cr}(\eta_{av}, \bar{\theta}_{av})$ is defined by (2.17), as mentioned above. Local material failure occurs when $I_f = 1$

2.5 Numerical integration of constitutive model

In a finite element environment, the solution is developed incrementally, and the constitutive equations are integrated at the element Gauss integration points. In every node, the unknowns are the displacement vector $\mathbf{u}$ and the non-local equivalent plastic strain e^p. Based on the state at the start of each increment, and the incremental displacements and non-local equivalent plastic strains ($\Delta\mathbf{u}$, Δe^p), we can obtain the history dependent behavior.

Let $\mathbf{F}$ denote the deformation gradient tensor, determined in terms of the nodal displacements within each finite element. At any given Gauss integration point, the values ($\mathbf{F}_n, \boldsymbol{\sigma}_n, \bar{\varepsilon}^p_n$, D_n, e^p_n) at time t_n, as well as the values ($\mathbf{F}_{n+1}, e^p_{n+1}$) at time $t_{n+1} = t_n + \Delta t$ are known, and we only have to determine ($\boldsymbol{\sigma}_{n+1}, \bar{\varepsilon}^p_{n+1}, D_{n+1}$). Subscript n denotes the value of each quantity at the start of the time increment ($t = t_n$), while subscript $n+1$ denotes the according value at the end of the time increment ($t = t_{n+1}$).

The time variation of $\mathbf{F}$ during the time increment $[t_n, t_{n+1}]$ can be written as

$$\mathbf{F}(t) = \Delta\mathbf{F}(t) \cdot \mathbf{F}_n = \mathbf{R}(t) \cdot \mathbf{U}(t) \cdot \mathbf{F}_n, \quad t_n \leqslant t \leqslant t_{n+1} \tag{2.26}$$

where $\Delta\mathbf{F}(t)$ is the deformation gradient at the start of the increment and $\mathbf{R}(t)$ and $\mathbf{U}(t)$ are the rotation and right stretch tensors associated with $\Delta\mathbf{F}(t)$. The following equations give the corresponding deformation rate $\mathbf{D}(t)$ and spin $\mathbf{W}(t)$ tensors:

$$\mathbf{D}(t) \equiv [\dot{\mathbf{F}}(t) \cdot \mathbf{F}^{-1}(t)]_s = [\Delta\dot{\mathbf{F}}(t) \cdot \Delta\mathbf{F}^{-1}(t)]_s, \tag{2.27}$$

and

$$\mathbf{W}(t) \equiv [\dot{\mathbf{F}}(t) \cdot \mathbf{F}^{-1}(t)]_\alpha = [\Delta\dot{\mathbf{F}}(t) \cdot \Delta\mathbf{F}^{-1}(t)]_\alpha, \tag{2.28}$$

where s and α denote the symmetric and anti-symmetric parts of a tensor.

Using the rotation tensor, introduced in (2.26), we can define the so-called "rotation-neutralized quantities" $\widehat{\boldsymbol{\sigma}}(t)$, $\hat{\mathbf{N}}^{(i)}(t)$ and $\hat{\mathbf{M}}(t)$ (Nagtegaal and Veldpaus, 1984 [13]):

$$\widehat{\boldsymbol{\sigma}}(t) = \mathbf{R}^T(t) \cdot \boldsymbol{\sigma}(t) \cdot \mathbf{R}(t), \quad \widehat{\mathbf{N}}(t) = \mathbf{R}^T(t) \cdot \mathbf{N}(t) \cdot \mathbf{R}(t), \quad \widehat{\mathbf{M}}(t) = \mathbf{R}^T(t) \cdot \mathbf{M}(t) \cdot \mathbf{R}(t). \tag{2.29}$$

We can assume that, in the time interval $[t_n, t_{n+1}]$, the Langragian triad associated with $\Delta\mathbf{F}(t)$ (i.e., the eigenvectors of $\mathbf{U}(t)$ remains fixed. Then, it can be shown that:

$$\mathbf{D}(t) = \mathbf{R}(t) \cdot \dot{\mathbf{E}}(t) \cdot \mathbf{R}^T(t), \quad \overset{\triangledown}{\boldsymbol{\sigma}}(t) = \mathbf{R}(t) \cdot \dot{\widehat{\boldsymbol{\sigma}}}(t) \cdot \mathbf{R}^T(t), \tag{2.30}$$

where $\mathbf{E}(t) = \ln\mathbf{U}(t)$ is the logarithmic strain relative to the configuration at t_n.
Note that at the start of the time increment ($t = t_n$):

$$\mathbf{F}_n = \mathbf{R}_n = \mathbf{U}_n = \boldsymbol{\delta}, \quad \widehat{\sigma}_n = \sigma_n, \quad \mathbf{E}_n = \mathbf{0}, \tag{2.31}$$

whereas at the end of the time increment ($t = t_{n+1}$)

$$\Delta\mathbf{F}_{n+1} = \mathbf{F}_{n+1} \cdot \mathbf{F}_n^{-1} = \mathbf{R}_{n+1} \cdot \mathbf{U}_{n+1} = \text{known, and} \qquad \mathbf{E}_{n+1} = \ln\mathbf{U}_{n+1} = \text{known.} \tag{2.32}$$

$\widehat{\boldsymbol{\sigma}}$ and $\boldsymbol{\sigma}$ have the same invariants, and $\mathbf{P}$ is an isotropic function of its arguments. With these in mind, the *rate-independent* elastoplastic equations can be written as:

$$\dot{\mathbf{E}} = \dot{\mathbf{E}}^e + \dot{\mathbf{E}}^p, \tag{2.33}$$

$$\dot{\widehat{\boldsymbol{\sigma}}} = \boldsymbol{\mathcal{L}}^e : \dot{\mathbf{E}}^e = \boldsymbol{\mathcal{L}}^e : (\dot{\mathbf{E}} - \dot{\mathbf{E}}^p), \tag{2.34}$$

$$\Phi(p, \sigma_e, \theta, \bar{\varepsilon}^p, D) = 0, \tag{2.35}$$

$$\dot{\mathbf{E}}^p = \dot{\lambda}\mathbf{P}(\widehat{\boldsymbol{\sigma}}, \bar{\varepsilon}^p, D) = \dot{\lambda}\left(\frac{1}{3}\frac{\partial\Phi}{\partial p}\boldsymbol{\delta} + \frac{\partial\Phi}{\partial\sigma_e}\widehat{\mathbf{N}} + \frac{1}{\sigma_e}\frac{\partial\Phi}{\partial\theta}\widehat{\mathbf{M}}\right), \tag{2.36}$$

$$\dot{\bar{\varepsilon}}^p = \sqrt{\frac{2}{3}\dot{\mathbf{E}}^p : \dot{\mathbf{E}}^p}. \tag{2.37}$$

The equation of evolution of damage is given by (2.22) and (2.23), while (2.36) shows that $\dot{\mathbf{E}}^p$ is co-axial with $\widehat{\boldsymbol{\sigma}}$.
The numerical integration of the above elastoplastic equations is as follows. Since the non-local equivalent plastic strain e^p is a nodal variable, its value is known at the Gauss integration points. The evolution of damage is first calculated with the use of a forward Euler scheme in (2.22) and (2.23). As the solution develops, the evolution of damage indicator I is monitored and we calculate:

$$I_{n+1} = I_n + \frac{\Delta\widehat{e}^p}{\bar{\varepsilon}_i^p(\eta_{av|n}, \bar{\theta}_{av|n})}. \tag{2.38}$$

When $I_{n+1} \geq 1$ for the first time, the corresponding value of $\sigma_{yi} = \sigma_y(\bar{\varepsilon}^p_{n+1})$ is stored. The damage evolution is calculated as:

$$\Delta D = \begin{cases} \frac{\sigma_{yi}}{G_f}\Delta\hat{e}^p & \text{if} \quad I_n \geq 1 \quad \text{and} \quad \eta_n > \eta_{cr} \quad \text{and} \quad D_n < D_{cr|n}, \\ 0 & \text{otherwise} \end{cases} \tag{2.39}$$

$$D_{n+1} = \min[D_n + \Delta D, D_{cr|n}] = \text{known}, \tag{2.40}$$

$$I_{f|n+1} = I_{f|n} + \frac{\Delta D}{D_{cr|n}} = \text{known}. \tag{2.41}$$

When $I_{f|n+1} = 1$, the material loses its load carrying capacity at that Gauss point. Equations (2.33) and (2.34) are integrated exactly:

$$\Delta\mathbf{E} = \Delta\mathbf{E}^e + \Delta\mathbf{E}^p, \tag{2.42}$$

$$\widehat{\boldsymbol{\sigma}}_{n+1} = \widehat{\boldsymbol{\sigma}}^e - \boldsymbol{\mathcal{L}}^e : \Delta\mathbf{E}^p = \widehat{\boldsymbol{\sigma}}^e - 2G\Delta\mathbf{E}^p - \Big(\kappa - \frac{2}{3}G\Big)\Delta E^p_{kk}\boldsymbol{\delta}, \tag{2.43}$$

where $\widehat{\boldsymbol{\sigma}}^e = \boldsymbol{\sigma}_n + \boldsymbol{\mathcal{L}}^e : \Delta\mathbf{E} =$ known, is the "elastic predictor" and the notation $\Delta A = A_{n+1} - A$ is used.
If the yield condition is not violated by the elastic predictor (i.e., $\Phi(\widehat{\boldsymbol{\sigma}}^e, \bar{\varepsilon}^p_n, D_n) \leq 0$, then:

$$\boldsymbol{\sigma}_{n+1} = \mathbf{R}_{n+1} \cdot \widehat{\boldsymbol{\sigma}}^e \cdot \mathbf{R}^T_{n+1}, \quad \bar{\varepsilon}^p_{n+1} = \bar{\varepsilon}^p_n, \quad D_{n+1} = D_n, \tag{2.44}$$

and the integration is completed.
If $\Phi(\widehat{\boldsymbol{\sigma}}^e, \bar{\varepsilon}^p_n, D_n) > 0$, then plastic deformation takes place and we can use a backward Euler scheme in order to numerical integrate the flow rule in (2.36):

$$\Delta\mathbf{E}^p = \Delta\lambda\mathbf{P}(\widehat{\boldsymbol{\sigma}}_{n+1}, \bar{\varepsilon}^p_{n+1}) = \Delta\lambda\left(\frac{1}{3}\frac{\partial\Phi}{\partial p}\boldsymbol{\delta} + \frac{\partial\Phi}{\partial\sigma_e}\widehat{\mathbf{N}} + \frac{1}{\sigma_e}\frac{\partial\Phi}{\partial\theta}\widehat{\mathbf{M}}\right)_{n+1}. \tag{2.45}$$

Lastly, the following expression determines the increment of the local equivalent plastic strain increment $\Delta\bar{\varepsilon}^p$:

$$\Delta\bar{\varepsilon}^p = \sqrt{\frac{2}{3}\Delta\mathbf{E}^p : \Delta\mathbf{E}^p}. \tag{2.46}$$

The integration algorithm is summarized in the following paragraph. The primary unknown quantities are $\Delta\lambda$ and $\Delta\mathbf{E}^p$ and the basic equations are the yield condition (2.35) and the plastic flow rule (2.45):

$$\Phi(\widehat{\boldsymbol{\sigma}}_{n+1}, \bar{\varepsilon}^p_{n+1}) = 0, \tag{2.47}$$

$$\Delta\mathbf{E}^p - \Delta\lambda\mathbf{P}(\widehat{\boldsymbol{\sigma}}_{n+1}, \bar{\varepsilon}^p_{n+1}) = 0. \tag{2.48}$$

In the equations above, $\widehat{\boldsymbol{\sigma}}_{n+1}$ and $\bar{\varepsilon}^p_{n+1}$ are determined in terms of $\Delta\mathbf{E}^p$:

$$\widehat{\boldsymbol{\sigma}}_{n+1}(\Delta\mathbf{E}^p) = \widehat{\boldsymbol{\sigma}}^e - 2G\Delta\mathbf{E}^p - \left(\kappa - \frac{2}{3}G\right)\Delta E^p_{kk}\boldsymbol{\delta}, \tag{2.49}$$

$$\bar{\varepsilon}^p_{n+1}(\Delta\mathbf{E}^p) = \bar{\varepsilon}^p_n + \sqrt{\frac{2}{3}\Delta\mathbf{E}^p : \Delta\mathbf{E}^p}. \tag{2.50}$$

Using Newton's method, we can solve (2.47) and (2.48) to find $\Delta\lambda$ and $\Delta\mathbf{E}^p$. In every iteration, for the current values of $\Delta\lambda$ and $\Delta\mathbf{E}^p$, we use the equations (2.49) and (2.50) to calculate $\widehat{\boldsymbol{\sigma}}_{n+1}$ and $\bar{\varepsilon}^p_{n+1}$. Finally, we compute $\boldsymbol{\sigma}_{n+1}$ from

$$\boldsymbol{\sigma}_{n+1} = \mathbf{R}_{n+1} \cdot \widehat{\boldsymbol{\sigma}}_{n+1} \cdot \mathbf{R}^T_{n+1}, \tag{2.51}$$

and the integration process is completed.

As the solution develops, the quantities $A \equiv \int_0^{\hat{e}^p} \eta d\hat{e}^p$ and $B \equiv \int_0^{\hat{e}^p} \bar{\theta} d\hat{e}^p$ are calculated and stored. More specifically, at the end of every increment, η_{av} and $\bar{\theta}_{av}$ are calculated and stored as follows:

$$\Delta A = \frac{\eta_n + \eta_{n+1}}{2}\Delta\hat{e}^p, \quad A_{n+1} = A_n + \Delta A, \quad \eta_{av|(n+1)} = \frac{A_{n+1}}{\hat{e}^p_{n+1}}, \tag{2.52}$$

$$\Delta B = \frac{\bar{\theta}_n + \bar{\theta}_{n+1}}{2}\Delta\hat{e}^p, \quad B_{n+1} = B_n + \Delta B, \quad \bar{\theta}_{av|(n+1)} = \frac{B_{n+1}}{\hat{e}^p_{n+1}}. \tag{2.53}$$

The computer implementation of the algorithm discussed above can be simplified, if the principal directions are used, as described in the following (see Simo, 1998 [16]; Aurrichio and Taylor, 1999 [2]; Borja *et al.*, 2003 [7]). From equation (2.45) we can conclude that $\Delta\mathbf{E}^p$ is co-axial with $\widehat{\boldsymbol{\sigma}}_{n+1}$, and from equation (2.49) we can conclude that $\widehat{\boldsymbol{\sigma}}^e$ is also co-axial with $\widehat{\boldsymbol{\sigma}}_{n+1}$. Thus, the eigenvectors $\hat{\mathbf{n}}^{(i)}$ of the (still unknown) tensors $\widehat{\boldsymbol{\sigma}}_{n+1}$ and $\Delta\mathbf{E}^p$ can be determined from the eigenvectors of the (known) elastic predictor $\widehat{\boldsymbol{\sigma}}^e$. Therefore, we can write:

$$\widehat{\boldsymbol{\sigma}}_{n+1} = \sum_{i=1}^{3} \sigma_i \hat{\mathbf{n}}^{(i)}\hat{\mathbf{n}}^{(i)} \quad \text{and} \quad \Delta\mathbf{E}^p = \sum_{i=1}^{3} \Delta E_i^p \hat{\mathbf{n}}^{(i)}\hat{\mathbf{n}}^{(i)} \tag{2.54}$$

and the problem reduces to the calculation of the principal components ΔE_i^p and σ_i. In this case, the primary unknowns are $\Delta\lambda$ and ΔE_i^p and equations (2.47) - (2.50) are simplified:

$$\Phi(\sigma_1, \sigma_2, \sigma_3, \bar{\varepsilon}^p_{n+1}) = 0, \tag{2.55}$$

$$\Delta\varepsilon_i^p - \Delta\lambda P_i(\sigma_1, \sigma_2, \sigma_3, \bar{\varepsilon}^p_{n+1}) = 0, \quad (i = 1, 2, 3), \tag{2.56}$$

where

$$\sigma_i(\Delta E_1^p, \Delta E_2^p, \Delta E_3^p) = \sigma_i^e - 2G\Delta E_i^p - \left(\kappa - \frac{2}{3}G\right)(\Delta E_1^p + \Delta E_2^p + \Delta E_3^p), \tag{2.57}$$

$$\bar{\varepsilon}^p_{n+1}(\Delta E_1^p, \Delta E_2^p, \Delta E_3^p) = \bar{\varepsilon}^p_n + \sqrt{\frac{2}{3}\left[(\Delta E_1^p)^2 + (\Delta E_2^p)^2 + (\Delta E_3^p)^2\right]}, \tag{2.58}$$

$$p = \frac{\sigma_1 + \sigma_2 + \sigma_3}{3}, \quad s_i = \sigma_i - p, \quad \sigma_e = \sqrt{\frac{3}{2}(s_1^2 + s_2^2 + s_3^2)}, \tag{2.59}$$

$$J_3 = s_1 s_2 s_3, \quad \theta = \frac{1}{3}\arcsin\left(-\frac{27}{2}\frac{J_3}{\sigma_e^3}\right), \quad \theta_i = \theta + (5 - 4i)\frac{\pi}{6}, \tag{2.60}$$

$$N_i = \cos\theta_i, \quad M_i = -\sin\theta_i, \quad P_i = \frac{1}{3}\frac{\partial\Phi}{\partial p} + \frac{\partial\Phi}{\partial\sigma_e}N_i + \frac{1}{\sigma_e}\frac{\partial\Phi}{\partial\theta}M_i. \tag{2.61}$$

The four unknowns $(\Delta\lambda, \Delta E_1^p, \Delta E_2^p, \Delta E_3^p)$ are calculated by solving the above system of **four** non - linear equations (2.54) and (2.55).

In the case of a *plastically incompressible material* ($\frac{\partial\Phi}{\partial p} = 0$ and D_{kk}^p), the problem is further simplified, as we can set ΔE_3^p = - $(\Delta E_1^p + \Delta E_2^p)$, eliminate $\Delta\lambda$ from (2.55) and use $(\Delta E_1^p, \Delta E_2^p)$ as the primary unknowns to find:

$$\Phi(\sigma_i, \bar{\varepsilon}_{n+1}^p) = 0, \tag{2.62}$$

$$\Delta E_1^p P_2(\sigma_i, \bar{\varepsilon}_{n+1}^p) - \Delta E_2^p P_1(\sigma_i, \bar{\varepsilon}_{n+1}^p) = 0, \tag{2.63}$$

where

$$\sigma_1(\Delta E_1^p) = \sigma_1^e - 2G\Delta E_1^p, \quad \sigma_2(\Delta E_2^p) = \sigma_2^e - 2G\Delta E_2^p, \tag{2.64}$$

$$\sigma_3(\Delta E_1^p, \Delta E_2^p) = \sigma_3^e + 2G(\Delta E_1^p + \Delta E_2^p), \tag{2.65}$$

$$\bar{\varepsilon}_{n+1}^p(\Delta E_1^p, \Delta E_2^p) = \bar{\varepsilon}_n^p + \sqrt{\frac{4}{3}\left[(\Delta E_1^p)^2 + (\Delta E_2^p)^2 + \Delta E_1^p \Delta E_2^p\right]}. \tag{2.66}$$

The problem now reduces to just solving **two** non-linear equations (2.62) and (2.63), to find $(\Delta E_1^p, \Delta E_2^p)$.

2.6 Non-local dynamic problems in ABAQUS/explicit via "VUMAT"

Solutions in *dynamic* problems which include inertia terms can be obtained by using the user material subroutine "VUMAT" in ABAQUS/Explicit together with a *DYNAMIC TEMPERATURE DISPLACEMENT analysis option. The process is described below:

In an isotropic material, the transient heat transfer equation, as solved in ABAQUS is:

$$k\nabla^2 T + r(\Delta\boldsymbol{\varepsilon}, T) = \rho c\dot{T}, \tag{2.67}$$

where T is the temperature, k is the thermal conductivity, r is the heat supply per unit volume, $\Delta\boldsymbol{\varepsilon}$ is a strain increment properly defined in terms of nodal displacements (see ABAQUS manual [1] and Hughes and Winget, 1980 [9]), ρ is the material's density and c is the specific heat.
Comparing (2.67) with (2.19), we can identify the non-local equivalent plastic strain with

the temperature field in the coupled temperature-displacement ABAQUS analysis, using the following correspondence:

$$T \leftrightarrow e^p, \quad k \leftrightarrow \ell^2, \quad r(\Delta\boldsymbol{\varepsilon}(\mathbf{u}), T) \leftrightarrow \bar{\varepsilon}^p(\mathbf{u}, e^p) - e^p. \tag{2.68}$$

Also, c is given a small value, so that the transient term on the right hand side of (2.67) becomes negligible.
The constitutive equations are integrated numerically in VUMAT, however because r cannot be identified in VUMAT we use and the following "loading card" in ABAQUS/explicit:

*DFLUX
ALLEL, BFNU

where ALLEL is the set of all finite elements in the mesh, and BFNU signifies a user-defined heat supply per unit volume r (BFNU = **B**ody **F**lux **N**on **U**niform). As mentioned before, the value of c should be small, in order for the right hand side of (2.67) to be negligible. It can be shown that the value of c chosen should satisfy the following relation:

$$\rho c\dot{\varepsilon} < 10^{-4}, \tag{2.69}$$

where $\dot{\varepsilon} = \sqrt{\frac{2}{3}\dot{\mathbf{e}} : \dot{\mathbf{e}}}$ and $\dot{\mathbf{e}}$ is the deviatoric strain rate. The value of $r = \bar{\varepsilon}^p - e^p$ is defined in user subroutine VDFLUX, in which the value of e^p is provided as "temperature" and the value of $\bar{\varepsilon}^p$ is supplied by VUMAT via a user introduced COMMON block.

Chapter 3

Applications and F.E calculations

The theory presented above can be used, among others, in a very useful application; the Crash Box Impact Test. In this chapter, a basic description of the Crash Box Impact Test is given, followed by the numerical analysis of the model and some useful results deriving from it.

3.1 The Crash Box Impact Test

The crash box is a structure integrated in the front and back bumpers of vehicles, with a main purpose of dissipating the kinetic energy of the vehicle in case of a low speed collision, thus making the vehicle safer for the passengers and reducing repair costs.

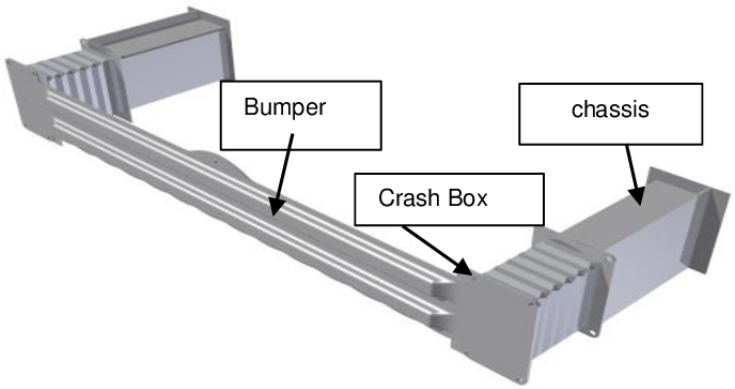

Figure 3.1: An assembly of bumper and two crash boxes, connected to the chassis. [10]

In order to ensure the efficacy of the aforementioned structure, an impact test which examines its deformation mode under dynamic impact loading is deemed necessary. This test is very similar to the Drop Weight Tear Test, in the sense that it is performed with the use of a drop tower device (Figure 3.2), which includes a falling mass (hammer) that can be up to 200 kg. The crash box is placed on a certain area (load cell) and is fixed on its bottom, usually with the aid of special equipment for stabilization (Figure 3.3). The falling

mass is dropped from a specific height (usually 10 to 12 meters, depending on the tower), reaching a terminal velocity upon impact of about 12-13 m/s and hits the center of a plate that is supported on the top of the crash box, resulting in the deformation mode presented in Figure 3.3. To fully capture the deformation evolution of the structure, a high-speed camera shall be used.

Figure 3.2: Drop tower. Source: Toolkit for the Design of Damage Tolerant Microstructures. [12]

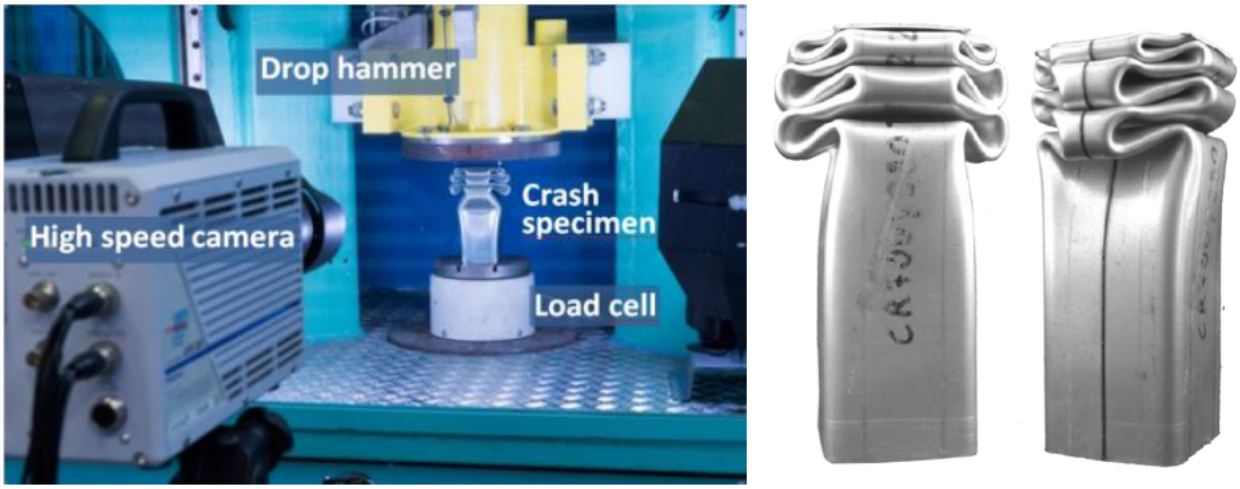

Figure 3.3: Equipment for the crash box impact test (left) and deformed state of the crash box (right). Source: Toolkit for the Design of Damage Tolerant Microstructures. [12]

3.2 Numerical analysis

The main subject of this thesis, as mentioned before, was the analysis of the Crash Box Impact Test, based on the theories described in Chapter 2. For this purpose, a series of finite element calculations has been carried out using both the local and non-local (gradient) versions of the damage constitutive model. The main goal of these simulations was to thoroughly examine the effect of the non-local formulation on the accuracy of the results produced by the FEM solution. The numerical analyses were carried out on ABAQUS/Explicit.

3.2.1 Model description

Concerning the geometry, the crash box consists of a hollow, rectangular shaped, steel tube, 330 mm long, 60 mm wide and 1.5 mm thick, with a U-type indentation on the upper part of two opposite sides and a thin steel plate that is attached to the top face of the tube. This design is based on the European Project "TOOLKIT for Damage Tolerant Micro-structure Design" [12]. The exact geometry and dimensions of the structure are presented in Figures 3.4 and 3.5. Regarding the boundary conditions, the structure is fixed on its bottom face ($u_x = u_y = u_z = 0$), with y being the axis parallel to the longitudinal axis of the crash box. The top face is restricted from rotation and free to move only in the y- direction and the lateral faces are free. An initial velocity $v = 12.522$ m/s, parallel to the y-axis is imposed at the center of the steel plate that is attached to the top face (this simulates a hammer falling and exerting an impact force, similar to the DWTT). In Figures 3.6, 3.7 and 3.8 the isotopic, top, and side views of the upper part of the crash box are presented, while Figure 3.9 depicts the CAE model assembly of the crash box with the attached steel plate. Due to the symmetries of the problem on planes xy and yz, one quarter of the model is shown in Figure 3.9 and all the contour plots that follow.

In the analysis of the models, a pressure-independent form of the yield function 2.4 due to Bai and Wierzbicki (2008) [5], as modified by Lian *et al.*(2012) [11] is used:

$$\Phi(\sigma_e, \theta, \bar{\varepsilon}^p, D) = \sigma_e - (1 - D)F\Big(\gamma(\theta)\Big)\sigma_y(\bar{\varepsilon}^p) = 0, \tag{3.1}$$

where

$$F(\gamma(\theta)) = c_\theta^s + (c_\theta^{ax} - c_\theta^s)\left[\gamma(\theta) - \frac{\gamma^{m+1}(\theta)}{m+1}\right], \tag{3.2}$$

$$\gamma(\theta) = \frac{\sqrt{3}}{2 - \sqrt{3}}\left(\frac{1}{\cos\theta} - 1\right), \tag{3.3}$$

$$c_\theta^{ax} = \begin{cases} c_\theta^t & \text{if} \quad \bar{\theta} \geq 0 \\ c_\theta^c & \text{if} \quad \bar{\theta} < 0 \end{cases}, \tag{3.4}$$

where $(c_\theta^s, c_\theta^t, c_\theta^c, m, n)$ are dimensionless material constants and the flow stress σ_y is a function of the equivalent plastic strain $\bar{\varepsilon}^p$: $\sigma_y(\bar{\varepsilon}^p) = \sigma_0\left(1 + \frac{\bar{\varepsilon}^p}{\varepsilon_0}\right)^{\frac{1}{n}}$, where σ_0 is the yield stress of the material (typical value $\sigma_0 = 330$ MPa), E is the elastic Young's modulus, $\varepsilon_0 = \frac{\sigma_0}{E}$ and $n \in [1, \infty)$ is the hardening exponent ($n \to \infty$ for a perfect plastic material). The length units are mm and E and σ_y are normalized dividing their original values with σ_0.
The yield function (3.1) can also be written as

$$F(\sigma_e, \theta, \bar{\varepsilon}^p, D) = \Sigma_e(\sigma_e, \theta, D) - \sigma_y(\bar{\varepsilon}^p) = 0, \tag{3.5}$$

where

$$\Sigma_e(\sigma_e, \theta, D) = \frac{\sigma_e}{(1 - D)F(\gamma(\theta))}. \tag{3.6}$$

The material properties, as well as the constants used in the calculations are presented in Tables 3.1 and 3.2. The density of common steel $\rho = 7850$ kg/m^3 is used in the calculations.

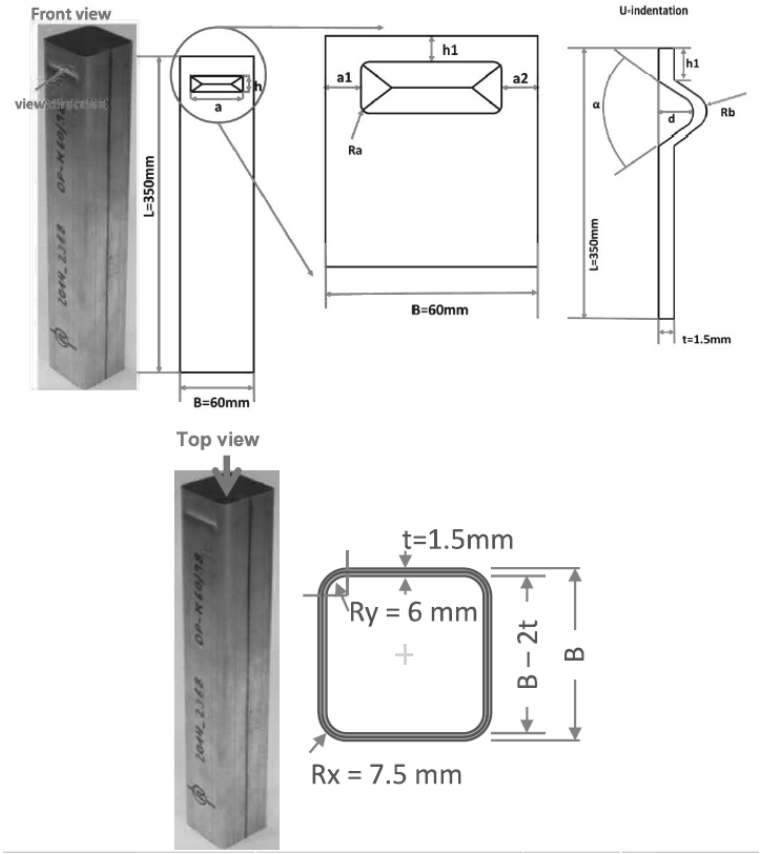

Figure 3.4: Geometry of the crash box

	Comments	Label*	Specimen	
Profile geometry	Profile length	L	330 mm	
	Profile width	B	60 mm	
	Profile thickness	t	1.5 mm	
	Profile bending radius (outside)	Rx	7.5 mm	
	Profile bending radius (inside)	Ry	6 mm	
Indentations **			1	2
Indentation location	Distance between profile top edge and the indentation upper edge	h1	22 mm	22 mm
	Distance between profile left edge and the indentation left edge	a1	10 mm	10 mm
	Distance between profile right edge and the indentation right edge	a2	10 mm	10 mm
Indentation geometry	Indentation length	a	40 mm	40 mm
	Indentation height	h	~ 4 mm	~ 4 mm
	Indentation round angle radius	R1	no spec.	no spec.
	Indentation depth	d	1.5 mm	1.5 mm
	Indentation opening angle	α	90 °	90 °
	Indentation radius (if U-type is used)	R2	1 mm	1 mm

Figure 3.5: Dimensions of the crash box

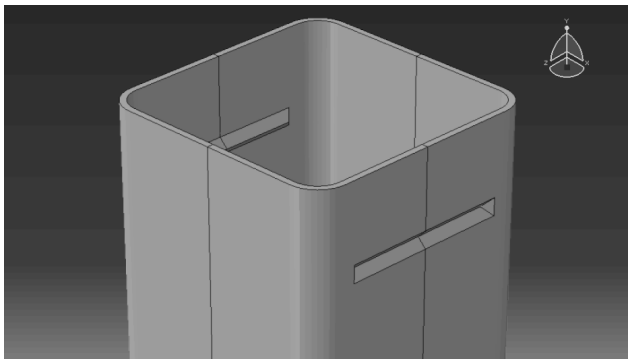

Figure 3.6: Isotopic view of the upper part of the crash box

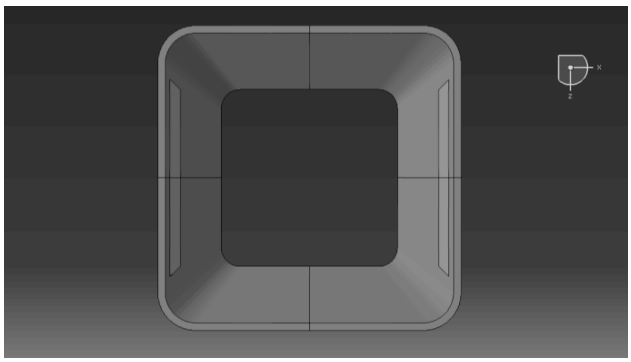

Figure 3.7: Top view of the upper part of the crash box

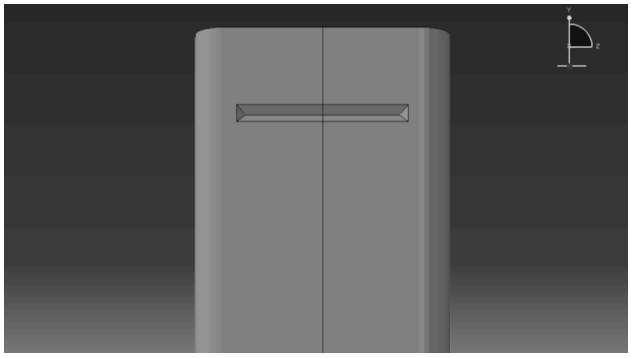

Figure 3.8: Side view of the upper part of the crash box

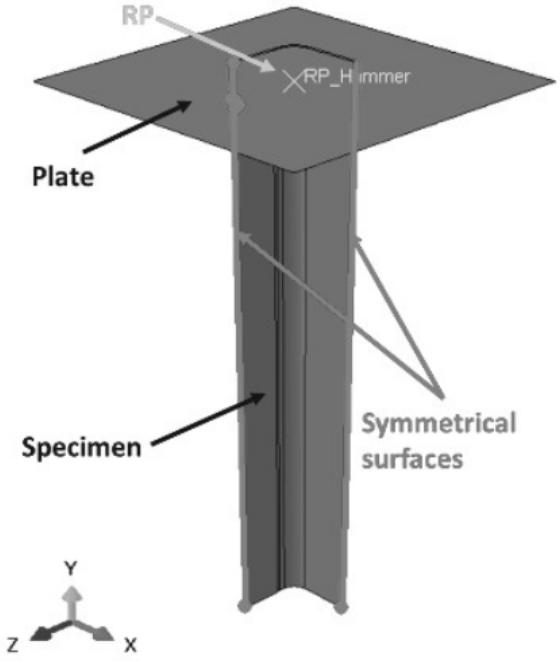

Figure 3.9: Crash box and steel plate assembly (one-quarter)

E/σ_0	ν	n	m	η_{cr}	c_θ^s	c_θ^t	c_θ^c
606.06	0.3	10	7	-0.33	0.95	1	0.98

Table 3.1: Material properties and constants

c_1	c_2	c_3	c_4	c_5	c_6	c_7	c_8
0.4943	2.266	0.10	1.131	0.83	0.5449	0.85	0.3926

Table 3.2: Values for the constants (c_1, c_2, ... ,c_8)

3.2.2 Results of the analysis

In general the problem is divided in two main parts:

- the space discretization, where the analysis is based on changes on the size of the elements of the mesh (mesh coarser or finer), while the time increments remain the same.
- the time discretization, where the size of the space elements remains the same, and all the changes are imposed on the time increments. This approach was considered since the problem is dynamic.

For the space discretization, both the local and non-local models are examined. For the time discretization, only the analysis of the non-local model with the coarse spatial mesh was deemed necessary. The main reasons for this are:

1. It was apparent, after examining the results of the space discretization, that the non-local model worked generally as the theory predicts, so it was fairly reasonable to assume it behaves the same in the time discretization as well. Therefore, the local model in the time domain was not analysed.
2. The time, as well as the computational power required for a complete analysis of the model with a fine spatial mesh are much larger than that of the corresponding coarse spatial mesh. For example, we observed that in the local model, the full coarse mesh analysis takes about 11 hours, while the full fine mesh analysis takes about 264 hours (more than 20 times longer). Thus, and taking into consideration that the required analysis time increases when we increase the number of increments, it was decided not to examine a fine spatial mesh for the case of time discretization.

After the numerical analysis was completed, for each model the values for the reaction force, contact force, kinetic energy and plastic dissipation energy in relation to the displacement were obtained, and the corresponding plots vs vertical displacement were created. Apart from that, contour plots for the ABAQUS/Explicit variables S.Mises, SDV1 and SDV11 were generated. S.Mises denotes the von Mises equivalent stress $\sigma_e = \sqrt{\frac{3}{2}\boldsymbol{s} : \boldsymbol{s}}$, where $\boldsymbol{s}$ is the deviatoric stress tensor. SDV1 denotes the equivalent plastic strain (ε^p for the local and e^p for the non-local model) and SDV11 the damage parameter (or "damage indicator") D, where D must always be less or equal to unity, as discussed in Chapter 2.

3.2.2.1 Space discretization

In the case of space discretization, two different types of mesh were used:

- a coarse mesh that consists of 54989 elements, and
- a fine mesh that consists of 2171179 elements.

The element type [1] was:

- for the local model: C3D8R (8-node linear brick, reduced integration, hourglass control)
- for the non-local model: C3D8RT (8-node thermally coupled brick, trilinear displacement and temperature, reduced integration, hourglass control)

Regarding the incrementation, 2.5 million time increments were used in this analysis for both models. The total time of the deformation (from $u = 0$ until u takes its final value) for the local and non-local models, for each mesh, is presented in the following table:

Model	Local coarse	Local fine	Non-local coarse	Non-local fine
Total time (ms)	10	11.6	14	11.878

Table 3.3: Total time of deformation for the two models (coarse and fine mesh).

Plots of Forces And Energies

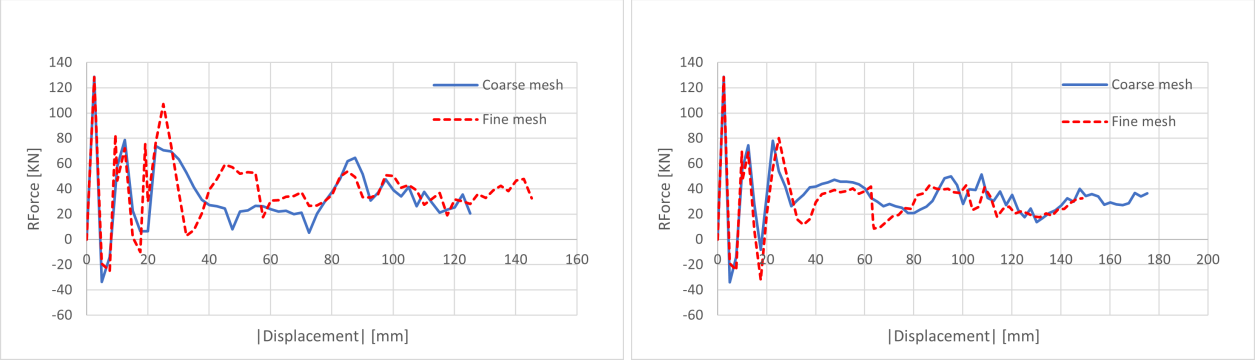

Figure 3.10: Reaction Force - Displacement plots for local (left) and non-local (right) models

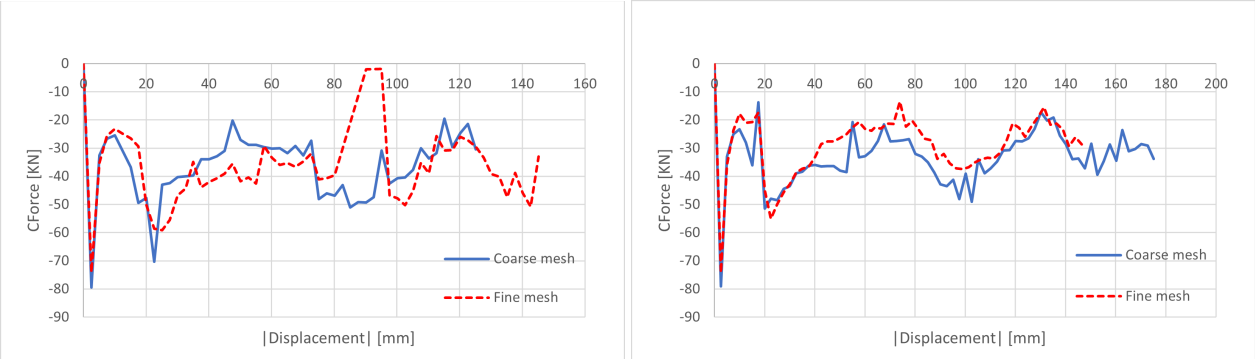

Figure 3.11: Contact Force - Displacement plots for local (left) and non-local (right) models

[1] (see ABAQUS 6.14 Documentation [1] for more details)

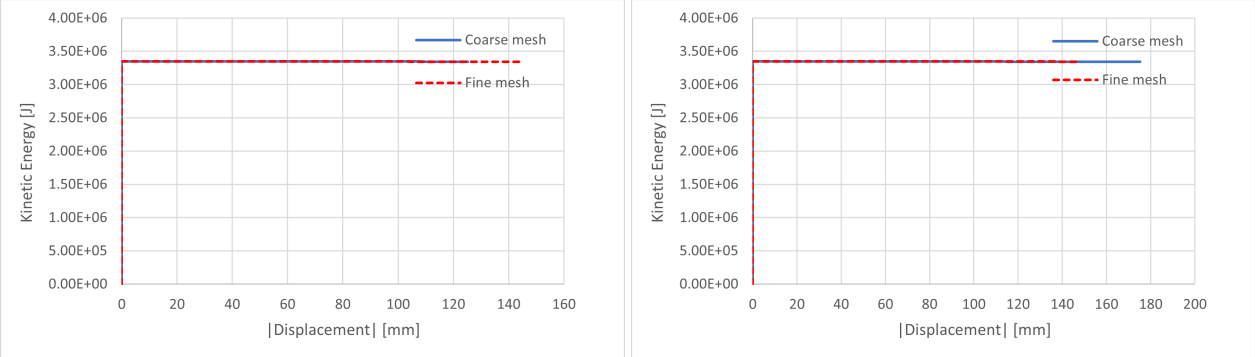

Figure 3.12: Kinetic Energy - Displacement plots for local (left) and non-local (right) models

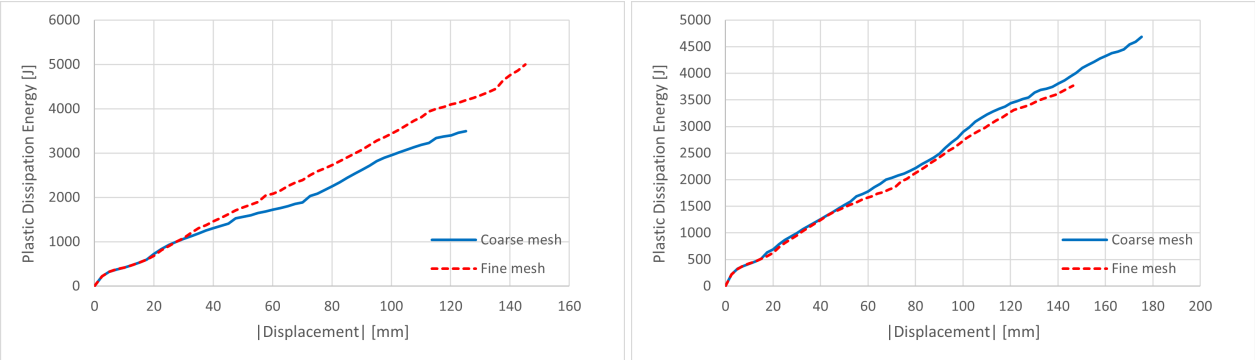

Figure 3.13: Plastic Dissipation Energy - Displacement plots for local (left) and non-local (right) models

Comments

1. In Figure 3.10, some differences on the reaction force - displacement curves between coarse and fine mesh for displacements between 20 and 80 mm can be observed in the local model. These differences seem to be significantly smaller in the case of the non-local model, however there are still some deviations between the coarse and the fine mesh, especially for displacements close to 30 - 40 mm and 60 - 70 mm.

2. In Figure 3.11, we notice some deviations between the coarse and the fine mesh in the local model, which are corrected in a satisfying degree in the non-local model, especially after $u \simeq 105$ mm. Again, there are some divergent areas ($u = 40 \sim 55$ mm and $u = 75 \sim 105$ mm), but the improvement is substantial.

3. In Figure 3.12, the kinetic energy - displacement lines for the coarse and fine mesh, for both the local and non-local model are identical. In both models the kinetic energy has the same constant value of 3.35 MJ.

4. In Figure 3.13, the deviation noticed in the case of the local model is almost completely eliminated in the non-local model. It is worth noting that the plastic dissipation energy has a maximum value of about 5 KJ, almost 1000 times lower than the (constant)

kinetic energy. This can be attributed to the fact that the analysis is dynamic, which results in much greater values for the kinetic energy compared to the plastic dissipation.

Distribution of Field Variables

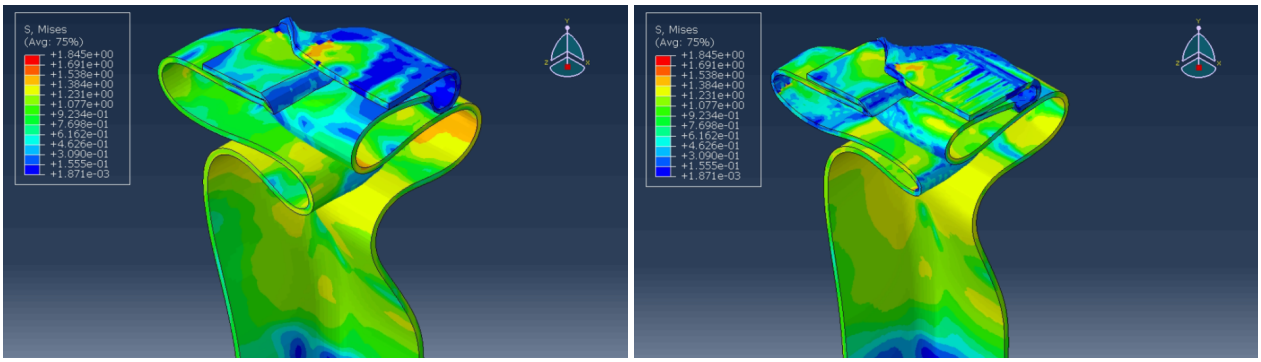

Figure 3.14: Local model. Von Mises equivalent stress σ_e for coarse (left) and fine (right) mesh at $u \simeq 125$ mm and t = 10 ms

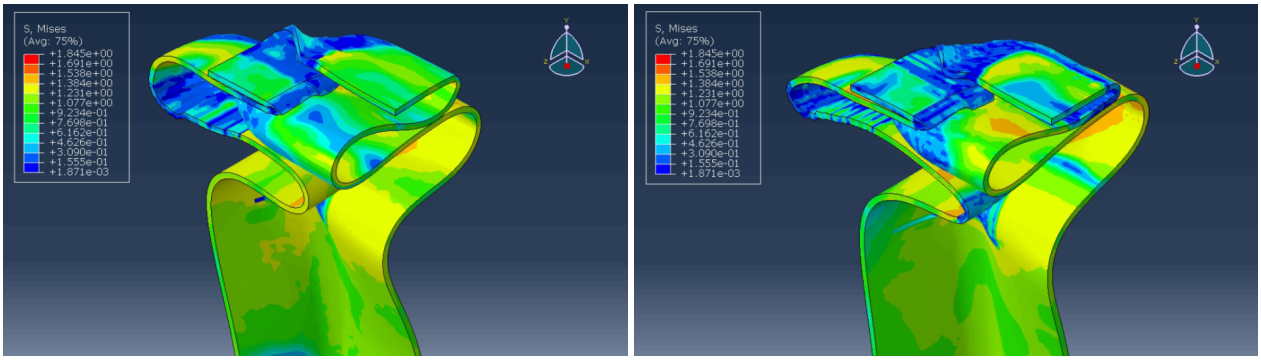

Figure 3.15: Non-local model. Von Mises equivalent stress σ_e for coarse (left) and fine (right) mesh at $u \simeq 125$ mm and t = 10 ms

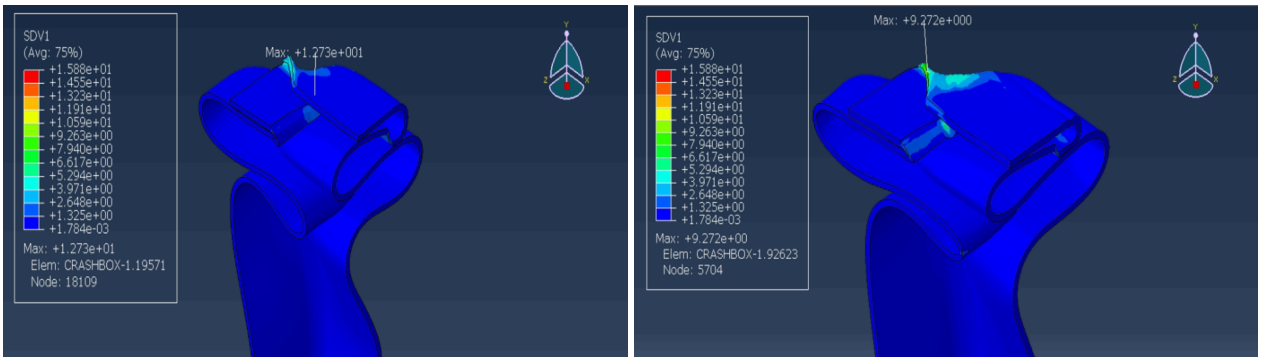

Figure 3.16: Local model. Equivalent plastic strain ε^p for coarse (left) and fine (right) mesh at $u \simeq 125$ mm and t = 10 ms

Figure 3.17: Non-local model. Equivalent plastic strain e^p for coarse (left) and fine (right) mesh at $u \simeq 125$ mm and t = 10 ms

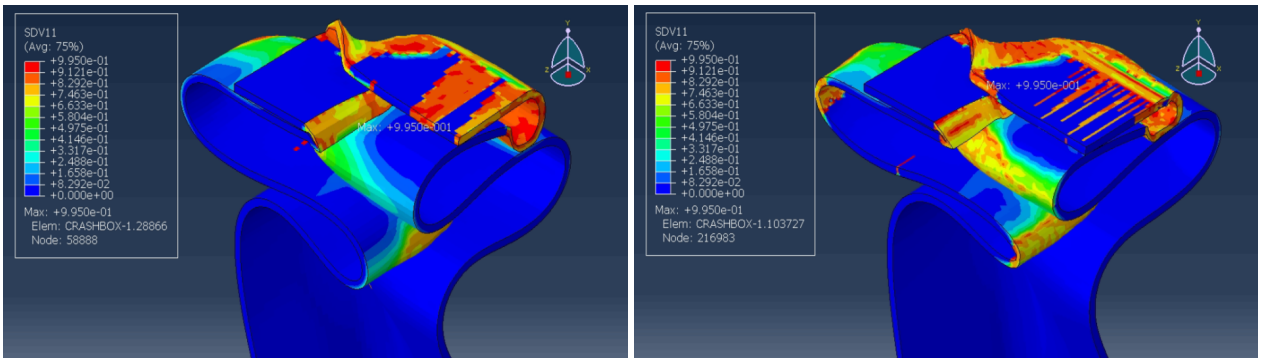

Figure 3.18: Local model. Damage parameter D for coarse (left) and fine (right) mesh at $u \simeq 125$ mm and t = 10 ms

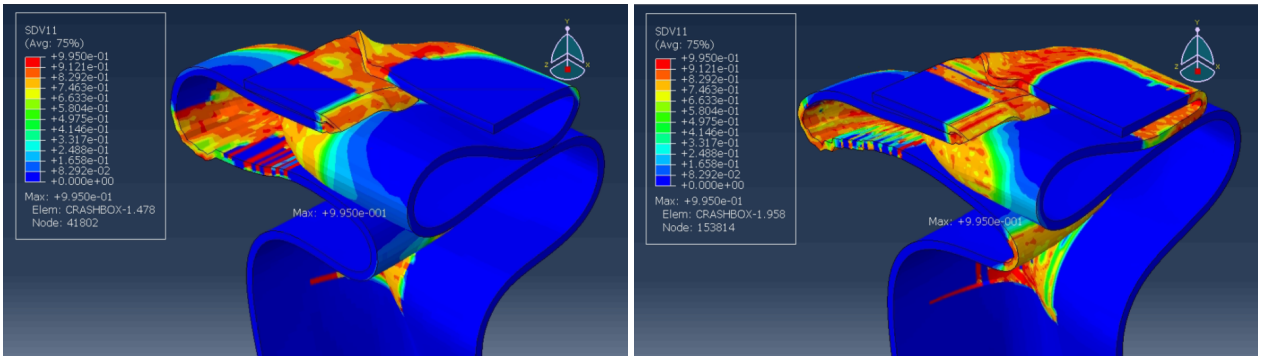

Figure 3.19: Non-local model. Damage parameter D for coarse (left) and fine (right) mesh at $u \simeq 125$ mm and t = 10 ms

Comments

Overall, we observe that in the non-local model, the deformation behavior between the coarse and the fine mesh is very similar, while in the local model, there are some differences in the way the structure "folds". Moreover, in the local model there are areas where the distribution of σ_e, ε^p and D have substantial differences (see Figures 3.14, 3.16 and 3.18), as opposed to the non-local model, where the contour plots are in better agreement.

3.2.2.2 Time discretization

In this part, the results of the non-local model, for coarse mesh and different time increments are presented. The four different cases of time discretization [2], along with the total time of deformation (from $u = 0$ until u takes its final value) for each case, are presented in the following table:

Number of increments	1.25 million	2.5 million	5 million	10 million
Total time (ms)	11.5	14	15	15

Table 3.4: Different cases of time discretization used and total time of deformation for each case.

Plots of Forces and Energies

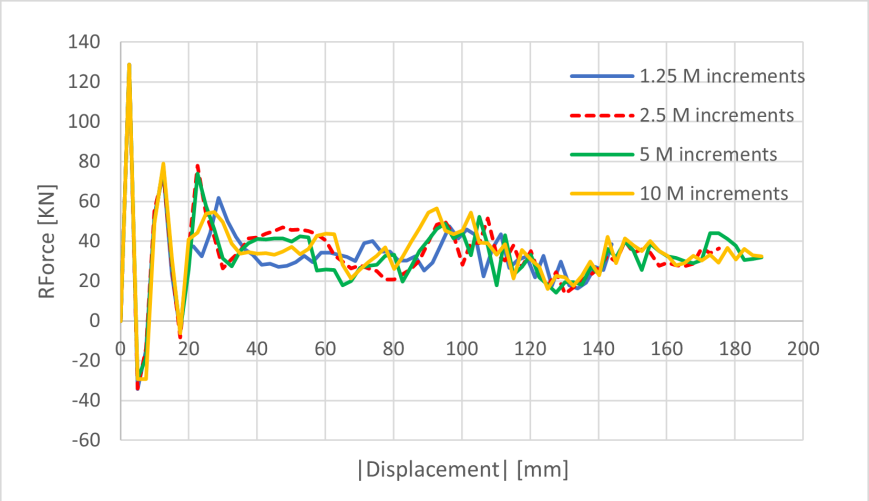

Figure 3.20: Reaction force - Displacement plot

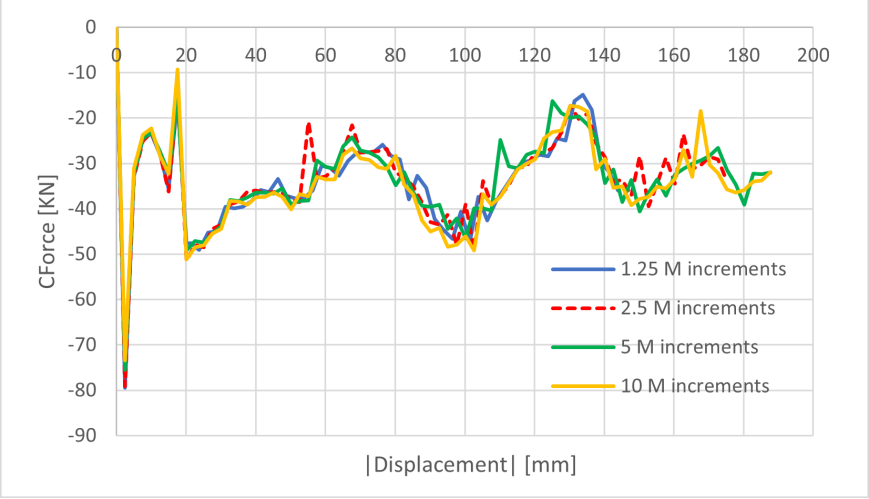

Figure 3.21: Contact force - Displacement plot

[2]From here on, M stands for "million" when referring to the number of increments.

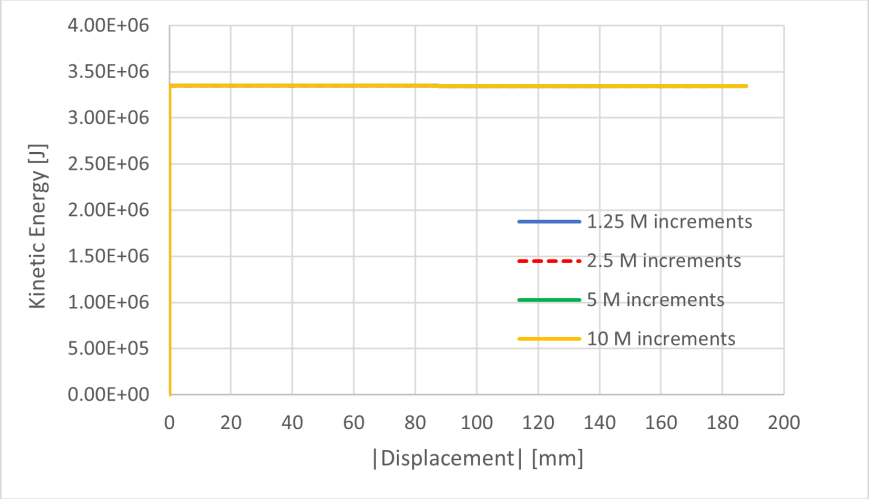

Figure 3.22: Kinetic Energy - Displacement plot

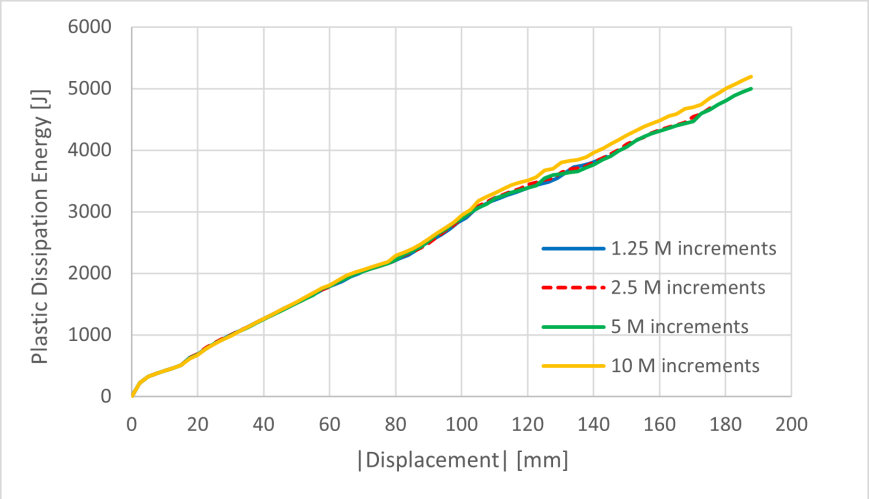

Figure 3.23: Plastic Dissipation Energy - Displacement plot

Comments

We can observe that the curves on the reaction force - displacement and contact force - displacement diagrams are very close for the different types of time discretization (Figures 3.20 and 3.21). There are some areas with larger deviations (i.e., Figure 3.20 for $u \simeq 25-100$ mm), but overall it seems that the non-local model works well in this case as well, especially for larger displacements, towards the end of the analysis. The kinetic energy has again the same constant value (3.35 MJ) in every case, and the plastic dissipation - displacement curves for each of the four types of time discretization are almost identical until about $u = 100$ mm, a point where they split, with the curve of 10M increments having a little greater values for the plastic dissipation energy. However the differences are very small and we can say that the curves converge.

Distribution of field variables

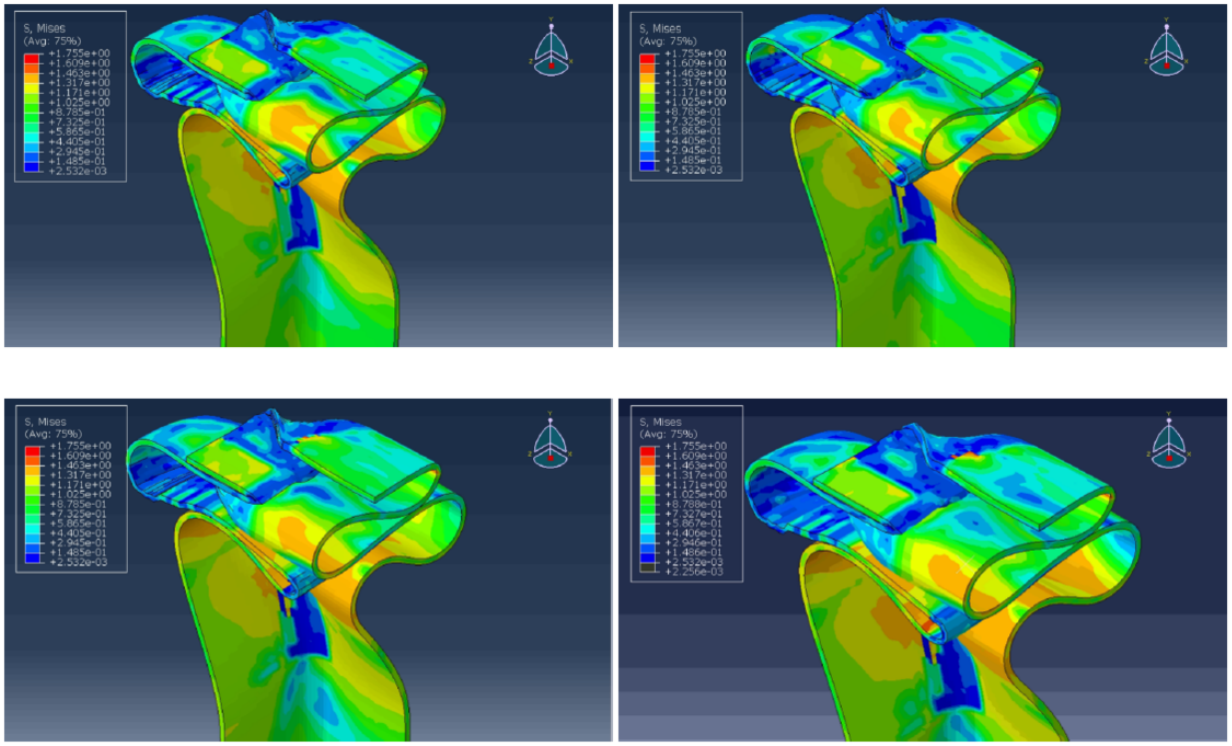

Figure 3.24: Von Mises equivalent stress σ_e for 1.25 M(upper left), 2.5 M(upper right), 5 M(lower left) and 10 M(lower right) increments, at $u \simeq 144$ mm and t = 11.6 ms

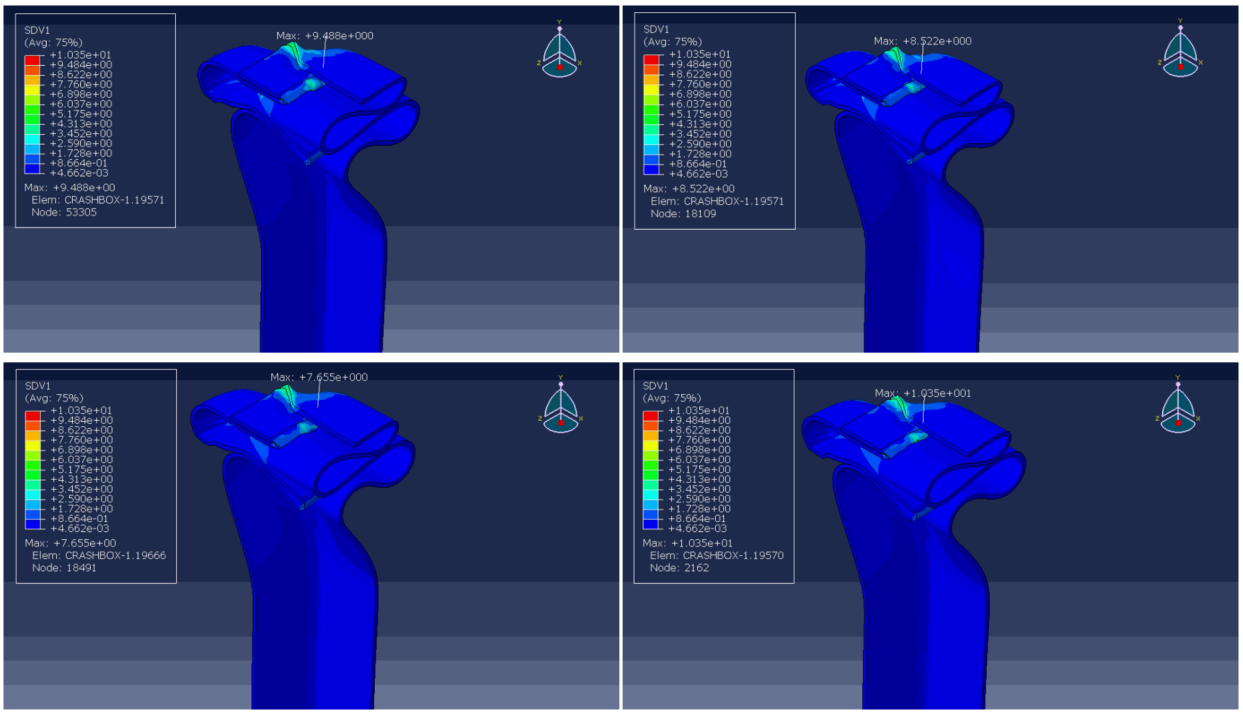

Figure 3.25: Equivalent plastic strain e^p for 1.25 M(upper left), 2.5 M(upper right), 5 M(lower left) and 10 M(lower right) increments, at $u \simeq 144$ mm and t = 11.6 ms

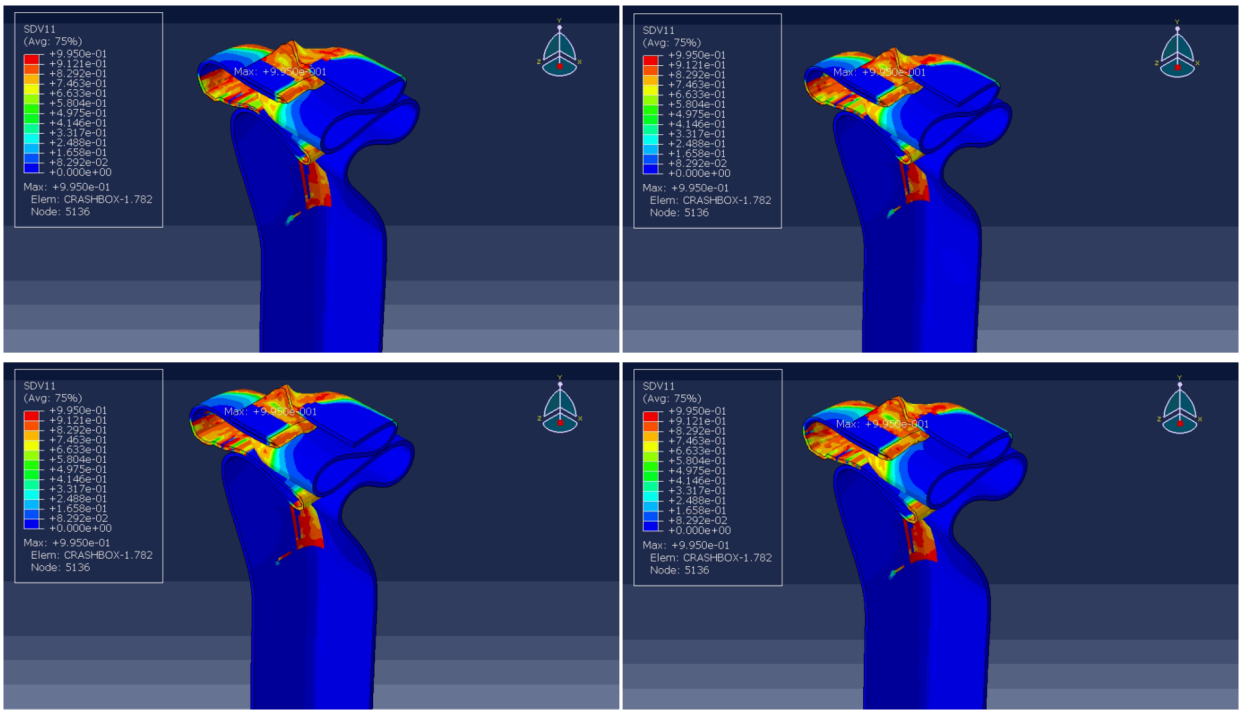

Figure 3.26: Damage parameter D for 1.25 M(upper left), 2.5 M(upper right), 5 M(lower left) and 10 M(lower right) increments, at $u \simeq 144$ mm and t = 11.6 ms

In general, once more, the deformation behavior of the crash box presented in Figures 3.24, 3.25 and 3.26 is very similar for each of the four cases of time discretization (the structure "folds" in the same way). Furthermore, the values of the variables of interest in each area of the structure are very close. Some more details can be observed in the 10 million increments case, which is reasonable, since the analysis is more detailed and the time steps are smaller, allowing for a better view on the actual solution.

General remark: An overview of the results of the simulations suggests that, the maximum values of equivalent plastic strain and damage parameter are noticed mainly on the top of the structure, in the area where the folds are sharper. Additionally, cracks are most likely to occur in these areas, especially in folded zones that correspond to the corners of the undeformed state as mentioned in [12], since these are the areas that receive most of the plastic deformation.

Chapter 4

Summary and Conclusions

As mentioned in the previous chapters, a significant issue we often encounter when trying to analyze the behavior of softening materials using the Finite Element Method is the fact that the classic (local) models do not take into consideration effects (i.e., force interactions) from regions far from the material point or region we examine. In an effort to overcome this problem, one approach is the use of the so-called non-local theories, which include long-distance interactions and can give us more reasonable and accurate results.

In the present thesis, a numerical analysis of the crash box impact test was conducted using a rate-independent local damage model and its corresponding non-local version, along with an effort to interpret the results based on the theory. The strain-gradient isotropic elastoplastic damage model of Papadioti *et al.*(2019) [14], that was based on the respective model of Bai and Wierzbicki (2008 [5], 2010 [6]) was used. The finite element calculations were carried out in ABAQUS/Explicit.

The effect of mesh refinement was examined for both the local and non-local model. The results for the basic variables of interest were obtained from ABAQUS and they were visualized in diagrams and contour plots, comparing the behavior of the two models according to the type of mesh. Apart from that, a basic simulation of the non-local model with a coarse spatial mesh was also carried out, with alterations in the number of time increments. Some basic conclusions following this study are:

- Regarding the space discretization, the non-local model behaves generally as expected, since it corrects to a big extent some major discrepancies of the local model between the coarse and the fine mesh. Some small deviations still exist, but especially at the end of the analysis, where the the displacement is bigger, the two types of mesh almost coincide. The non-local model also seems to predict better the deformation mode of the structure, since both coarse and fine mesh display very similar behavior, in contrast to the local model, where some differences in the way the crash box deforms are noticed.
- Regarding the time discretization, it is obvious that the non-local model once more gives accurate results, that are very close to the results of the corresponding non-local

model in the case of space discretization. Different types of time discretization don't seem to affect the results much, but it is certain that a smaller time step that results in more time increments can give more accurate predictions. Again, the deformation mode is almost identical for each case, something that is a direct result of the non-local effects.

To conclude, it is clear that the non-local theories find very useful application in cases where the numerical analyses do not produce accurate results, due to lack of consideration of long-distance effects in softening materials. However, in order to ensure the validity of these findings, the respective local model for the case of time discretization, a combination of different spatial meshes and number of time increments, as well as a practical experiment, would definitely be of use.

Bibliography

[1] ABAQUS, Analysis User's Manual, Version 6.14, © Dassault Systémes, 2014

[2] Auricchio, F. , Taylor, R.L. , 1999. A return-map algorithm for general associative isotropic elasto-plastic materials in large deformation regimes. Int. J. Plast. 15, 1359–1378

[3] Bai, Y. , Wierzbicki, T. , 2004a. A comparative study on various ductile crack formation criteria. J. Eng. Mater. Technol. 126, 314–324

[4] Bai, Y. , Wierzbicki, T. , 2005. On the cut-off value of negative triaxiality for fracture. Eng. Fract. Mech. 72, 1049–1069

[5] Bai, Y.L. , Wierzbicki, T. ,2008. A new model of metal plasticity and fracture with pressure and lode dependence. Int. J. Plast. 24, 1071–1096

[6] Bai, Y.L. , Wierzbicki, T. , 2010. Application of extended Mohr-Coulomb criterion to ductile fracture. Int. J. Fract. 161, 1–20

[7] Borja, R.A. , Sama, K.M. , Sanz, P.F. , 2003. On the numerical integration of three invariant elastoplastic constitutive models. Comput. Methods Appl. Mech. Eng 192, 1227–1258

[8] Engelen, R.A.B. , Geers, M.G.D. , Baaijens, F.P.T. , 2003. Nonlocal implicit gradient enhanced elasto-plasticity for the modelling of softening behaviour. Int. J. Plast. 19, 403–433

[9] Hughes, T.J.R. , Winget, J. , 1980. Finite rotation effects in numerical integration of rate constitutive equations arising in large-deformation analysis. Int. J. Numer. Methods Eng. 15, 1862–1867

[10] Kusyairi, I., 2017. The Influence of Origami and Rectangular Crash Box Variations on MPV Bumper with Offset Frontal Test Examination toward Deformability

[11] Lian, J. , Sharaf, M. , Archie, F. , Münstermann, S. , 2012. A hybrid approach for modelling of plasticity and failure behaviour of advanced high-strength steel sheets. Int. J. Damage Mech. 22, 188–218

[12] Liu, W. , Lian, J. , M*ü*nstermann, S. , Richter, H. , Pretorius, T. , Papadioti, I. , Bellas, I. , Tzini, M. , Kamoutsi, E. , Haidemenopoulos, G. , Aravas, N. , Cooreman, S. , Chandran,

S. , Verleysen, P. , Daniolos, N. , Tazedakis, A. , 2016 - 2017. Toolkit for the Design of Damage Tolerant Microstructures

[13] Nagtegaal, J.C. , Veldpaus, F.E. , 1984. On the implementation of finite strain plasticity equations in a numerical model. In: Pittman, J.F.T., Zienkiewicz, O.C., Wood, R.D., Alexander, J.M. (Eds.), Numerical Analysis of Forming Processes, papers presented at the international conference held at Swansea, UK, 12–16 July 1982. John Wiley and Sons Ltd., Chichester, pp. 351–371

[14] Papadioti, I. , Aravas, N. , Lian, J. , M*ü*nstermann, S. , 2019. A strain-gradient isotropic elastoplastic damage model with J_3 dependence

[15] Peerlings, R.H.J. , Geers, M.G.D. , Borstde, R. , Brekelmans, W.A.M. , 2001. A critical comparison of nonlocal and gradient-enhanced softening continua. Int. J. Solids Struct. 38, 7723–7746

[16] Simo, J.C. , 1998. Numerical analysis and simulation of plasticity. In: Ciarlet, P.G., Lions, J.L. (Eds.), Handbook of Numerical Analysis, Vol. VI. Elsevier Science B.V., pp. 183–499

[17] Wu, B. , Buchkremer, S. , Münstermann, S. , Lian, J. , Veselovac, D. , Bleck, W. , Klocke, F. , 2017a. Modeling of chip breakage in machining of AISI 1045 steel by using an improved damage mechanics model. Steel Res. Int. 88 . 1600338-n/a.

[18] Wu, B. , Li, X. , Di, Y. , Brinnel, V. , Lian, J. , Münstermann, S. , 2017b. Extension of the modified Bai–Wierzbicki model for predicting ductile fracture under complex loading conditions. Fatigue Fract. Eng. Mater. Struct. 40, 2152–2168

[19] Xenos, S., 2018. Computational Non-local Plasticity of Porous Metals (Diploma Thesis)